Cholinergic Afferent Stimulation Induces Axonal Function Plasticity in Adult Hippocampal Granule Cells

Highlights

- Cholinergic fiber stimulation caused a persistent reduction in the spike threshold

- Post-synaptic muscarinic receptor activation enhanced axonal $Ca_V3.2$ channel activity

- The sustained Ca^{2+} entry inhibited axonal K_V7 channels, lowering the spike threshold

- The lower spike threshold increased the propensity for action potential generation

Authors

Katiuscia Martinello, Zhuo Huang, ..., David A. Brown, Mala M. Shah

Correspondence

mala.shah@ucl.ac.uk

In Brief

Acetylcholine is thought to influence cognitive processing by affecting somato-dendritic excitability and neurotransmitter release. Here, Martinello et al. show that endogenous acetylcholine acts on axonal muscarinic receptors to significantly influence action potential initiation and information processing in hippocampal granule cells.

CrossMark

CellPress

Cholinergic Afferent Stimulation Induces Axonal Function Plasticity in Adult Hippocampal Granule Cells

Katiuscia Martinello,[1] Zhuo Huang,[1] Rafael Lujan,[2] Baouyen Tran,[3] Masahiko Watanabe,[4] Edward C. Cooper,[3] David A. Brown,[5] and Mala M. Shah[1,*]

[1]UCL School of Pharmacy, University College London, London, WC1N 1AX, UK
[2]Departamento de Ciencias Medicas, Universidad de Castilla-La Mancha, 02006 Albacete, Spain
[3]Neurology and Neuroscience, Baylor College of Medicine, TX 77030, USA
[4]Anatomy, Hokkaido University Graduate School of Medicine, Sapporo 060-8638, Japan
[5]Neuroscience, Physiology and Pharmacology, University College London, London, WC1E 6BT, UK
*Correspondence: mala.shah@ucl.ac.uk
http://dx.doi.org/10.1016/j.neuron.2014.12.030

SUMMARY

Acetylcholine critically influences hippocampal-dependent learning. Cholinergic fibers innervate hippocampal neuron axons, dendrites, and somata. The effects of acetylcholine on axonal information processing, though, remain unknown. By stimulating cholinergic fibers and making electrophysiological recordings from hippocampal dentate gyrus granule cells, we show that synaptically released acetylcholine preferentially lowered the action potential threshold, enhancing intrinsic excitability and synaptic potential-spike coupling. These effects persisted for at least 30 min after the stimulation paradigm and were due to muscarinic receptor activation. This caused sustained elevation of axonal intracellular Ca^{2+} via T-type Ca^{2+} channels, as indicated by two-photon imaging. The enhanced Ca^{2+} levels inhibited an axonal K_V7/M current, decreasing the spike threshold. In support, immunohistochemistry revealed muscarinic M1 receptor, $Ca_V3.2$, and $K_V7.2/7.3$ subunit localization in granule cell axons. Since alterations in axonal signaling affect neuronal firing patterns and neurotransmitter release, this is an unreported cellular mechanism by which acetylcholine might, at least partly, enhance cognitive processing.

INTRODUCTION

Acetylcholine is a neurotransmitter and neuromodulator in the CNS that has a salient role in cognition (Hasselmo and Sarter, 2011; Picciotto et al., 2012). Cholinergic afferents widely innervate the CNS. The medial septum projections to the hippocampus have been associated with cognitive processing. These are likely to be instrumental in mediating hippocampal neural network activity, such as theta-rhythm oscillations that are necessary for memory acquisition (Buzsáki, 2002). Moreover, altered acetylcholine receptor activity and cholinergic fiber lesions lower the threshold for hippocampal long-term potentiation, the cellular correlate of learning and memory (Hasselmo and Sarter, 2011; Picciotto et al., 2012). Hence, ascertaining how acetylcholine affects hippocampal neuronal excitability is vital for understanding cognitive processing.

The hippocampal dentate gyrus (DG) plays a fundamental role in processes such as memory encoding and storage (Acsády and Káli, 2007; Pelkey and McBain, 2008). Granule cells, the DG principal neurons, receive the primary input to the hippocampus from the cortex, which is relayed to hippocampal CA3 neurons via their axons (mossy fibers) (Acsády and Káli, 2007; Pelkey and McBain, 2008). The DG contains many inhibitory neurons (Coulter and Carlson, 2007). This, coupled with the unique granule cell somato-dendritic membrane properties (Krueppel et al., 2011; Lübke et al., 1998; Pernía-Andrade and Jonas, 2014), results in them having a very low mean action potential firing frequency rate in vivo (Henze et al., 2002; Pernía-Andrade and Jonas, 2014). Thus, only granule cells that receive a strong glutamatergic drive will participate in information transfer to the CA3 region (Acsády and Káli, 2007). A high density of cholinergic fibers, though, also innervates the DG (Aznavour et al., 2005). Interestingly, granule cells display action potential bursts during exploration-associated theta rhythms (Skaggs et al., 1996) when cholinergic neurons discharge maximally (Jones, 2004). However, relatively little is known about how cholinergic activity impacts DG cell function (Hasselmo and Sarter, 2011; Picciotto et al., 2012).

The cellular mechanisms by which acetylcholine exerts its effects are complex and are likely to depend on the timing of the release of acetylcholine as well as the state of neurons (Picciotto et al., 2012). Cholinergic receptor modulation of hippocampal pyramidal cell somato-dendritic excitability and synaptic plasticity has been extensively explored (Hasselmo and Sarter, 2011; Picciotto et al., 2012). Cholinergic fibers, however, innervate hippocampal cell axons too (Aznavour et al., 2005). The effects of acetylcholine on axonal signal processing remain to be elucidated. Understanding this is crucial as altered axonal information processing will impact neural firing patterns and synaptic release and, thereby, neural network excitability (Bean, 2007; Debanne et al., 2011; Kole and Stuart, 2012).

Here, we show that cholinergic fiber stimulation results in a persistent reduction of the granule cell action potential threshold and increased propensity to elicit action potentials. These effects are due to muscarinic receptor-induced sustained axonal Ca^{2+} influx via T-type Ca^{2+} channels, which then causes an enduring decrease in axonal K_V7 K^+ channel function, reducing the spike threshold. Hence, our results show that cholinergic afferent discharge primes granule cell axons to more readily elicit action potentials. This represents a unique means by which cholinergic afferent input enhances neuronal information processing and possibly influences memory formation.

RESULTS

Persistent Spike Threshold Reduction and Enhanced Excitability by Synaptically Released Acetylcholine

To investigate how endogenous acetylcholine affects granule cell intrinsic activity, we made patch-clamp recordings from mature cells in brain slices before and after extracellular stimulation of afferents in the stratum moleculare (Figure 1A). These cells had input resistances (R_N) of 297.94 ± 23.9 MΩ (n = 117) and complex dendritic trees (Figure 1A) as revealed by post hoc morphological analysis. Experiments were performed in the presence of glutamatergic and GABAergic ionotropic and metabotropic receptor inhibitors, unless otherwise stated.

Cholinergic fibers are most active during paradoxical sleep in vivo, firing in high-frequency bursts (average frequency of 16–29 spikes/s) (Brazhnik and Fox, 1999; Lee et al., 2005). We stimulated cholinergic fibers eight to ten times at an intra-burst frequency of 40 Hz and inter-burst interval of 125 ms (∼3 Hz; near theta frequency; average frequency = 27.8 Hz; Figure 1A). The stimulus strength was adjusted to yield single slow cholinergic synaptic potentials with amplitudes of 0.56 ± 0.1 mV (n = 15) and summation ratios of 2.49 ± 0.4 (n = 15; Figure 1A). This "high-frequency" (HF) stimulation paradigm was repeated ten times at 0.1 Hz. HF stimulation significantly lowered the action potential (spike) threshold, without affecting other intrinsic membrane properties (Figure 1B, Tables S1 and S2). This did not recover for up to 30 min after the stimulation. Consequently, granule cells generated more action potentials with depolarization (Figure 1B). Similar results were also obtained if the superfusate contained 1.3 mM Ca^{2+} concentrations (spike threshold decrease immediately and 30 min post-stimulation = 4.16 ± 0.6 mV and 5.00 ± 0.6 mV [n = 5]; Tables S1 and S2) instead of 2 mM Ca^{2+} (Figure 1B).

Cholinergic neurons, though, fire at lower frequencies in vivo during slow-wave sleep (average frequency of 0.8–1.9 spikes/s) (Lee et al., 2005; Simon et al., 2006). To mimic this, eight stimuli were delivered at 325 ms intervals (3.08 Hz) during 10 s (average frequency = 0.8 Hz; Figure S1A) and repeated ten times at 0.1 Hz. The initial synaptic potential amplitude (0.88 ± 0.2 mV, n = 6) and summation ratio (2.39 ± 0.3, n = 6) were similar to that with HF stimulation. This LF stimulation also reduced the action potential threshold and enhanced granule cell firing for at least 30 min, with other spike parameters or intrinsic membrane properties not affected (Figure S1 and Tables S1 and S2). Similar effects were observed if cholinergic fibers expressing channelrhodopsin and the fluorescent marker, eYFP, were optically stimulated at

0.8 Hz (protocol similar to LF electrical stimulation) with or without glutamate and GABA receptor blockers (Figure S2). Since LF optical or electrical stimulation effects were comparable to those produced by HF electrical stimulation, it implies that activation of a small population of acetylcholine receptors is sufficient to cause action potential threshold changes.

The granule cell action potential is initiated at the axon initial segment (AIS) (Schmidt-Hieber and Bischofberger, 2010), implying that cholinergic fiber stimulation caused axonal changes. This differed from previous reports indicating that cholinergic fibers affect somato-dendritic excitability in other hippocampal neurons (Buchanan et al., 2010; Cole and Nicoll, 1983; Gu and Yakel, 2011). One explanation might be that the released acetylcholine was degraded rapidly. To test this, we performed HF stimulation in the presence of the acetylcholinesterase inhibitor, neostigmine (3 μM). The cholinergic synaptic potential summation ratio (10.3 ± 3.6, n = 10) and the spike threshold decrease were significantly greater with neostigmine than in its absence (Figure S3). Additionally, neostigmine caused neuronal depolarization immediately after cholinergic afferent stimulation, which recovered within 10 min (Figure S3). Notwithstanding this, the primary effect of cholinergic afferent stimulation was to induce a long-term spike threshold reduction.

Enhanced Synaptic Potential-Spike Coupling and Spontaneous Action Potential Firing following Cholinergic Afferent Stimulation

We next asked whether the cholinergic afferent stimulation-induced spike threshold decrease might enhance excitatory synaptic potential-spike (E-S) coupling and spontaneous action potential firing. To elicit 50 Hz glutamatergic excitatory postsynaptic potential (EPSP) trains, we stimulated afferents onto granule cell dendrites before and after HF cholinergic fiber stimulation (Figure 1B) in the presence of GABA receptor inhibitors only. The stimulation strength was adjusted so that the EPSP summation was subthreshold (average first EPSP amplitude = 5.01 ± 1.4 mV, n = 6; Figure 1B). Following HF cholinergic afferent stimulation, the initial EPSP amplitude was comparable (5.24 ± 1.5 mV, n = 6) but 50 Hz EPSP trains now resulted in spikes (Figure 1B). This was not due to alterations in pre-synaptic function as subthreshold EPSPs generated using an injected α-waveform yielded spikes following HF cholinergic afferent stimulation (Figure 1B). Further, spontaneous action potential frequency recorded in a "loose" cell-attached mode was significantly enhanced for at least 25 min following HF cholinergic fiber stimulation (Figure 1B). Hence, cholinergic afferent stimulation enhances information processing in hippocampal granule cells by persistently reducing the spike threshold.

Cholinergic Afferent-Induced Long-Term Spike Threshold Plasticity Is Muscarinic Receptor Dependent

Next, we investigated whether muscarinic or nicotinic cholinergic receptors might cause the spike threshold changes. The slow synaptic potentials induced by HF and LF stimulation paradigms as well as the associated spike threshold reductions were inhibited by the muscarinic receptor antagonist, atropine (3 μM, Figure 1, Figure S1) but not by co-application of methyllycaconitine (an α7 receptor antagonist, 10 nM) (Alkondon et al.,
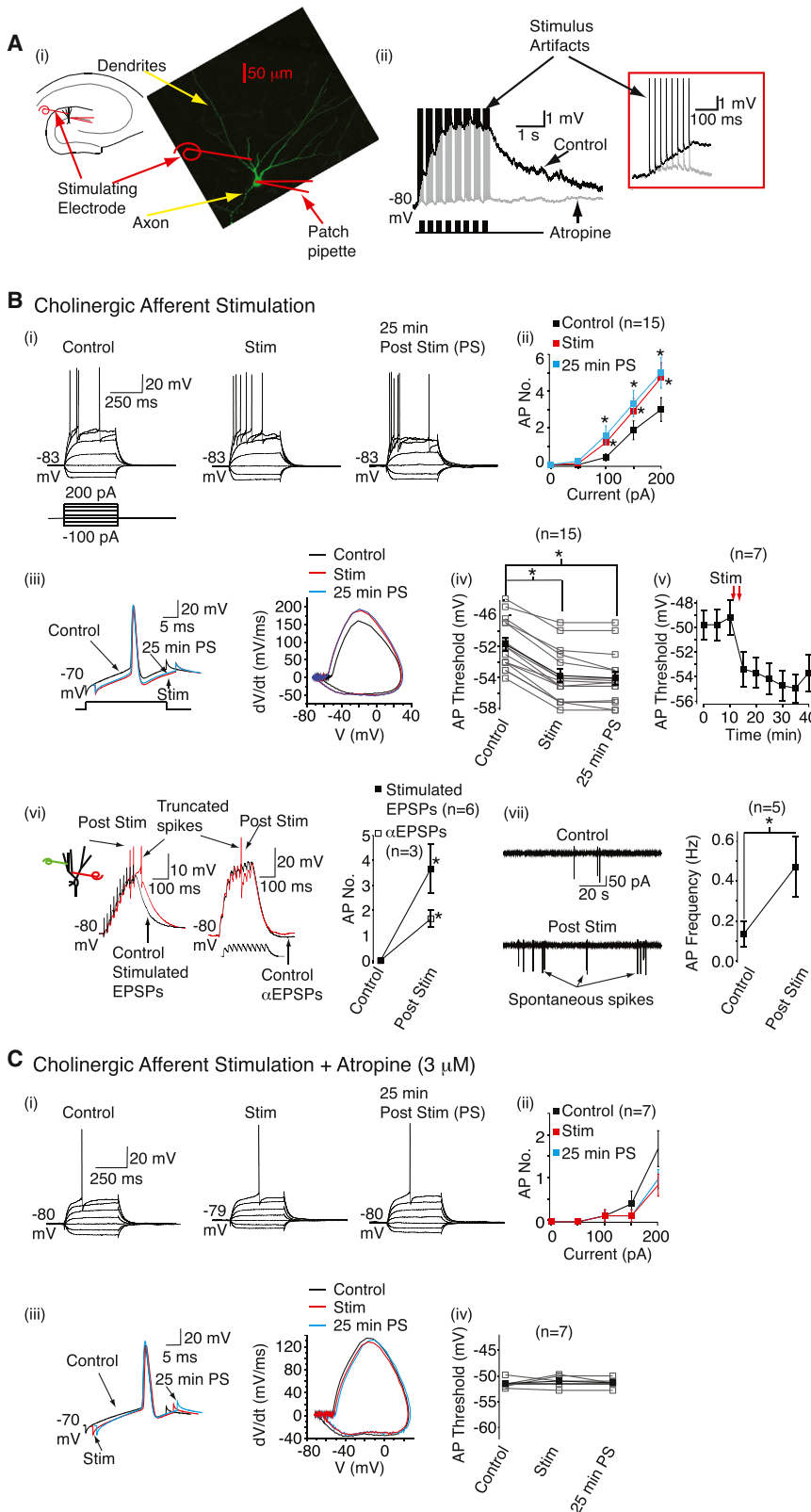
Figure 1. Endogenous Acetylcholine Release Enhances Granule Cell Excitability by Lowering the Action Potential Threshold

(Ai) Hippocampal slice preparation schematic and example image of granule cell. Scale bar, 50 μm.

(Aii) Representative slow excitatory synaptic potentials before and after atropine (3 μM). The first burst is shown on an expanded timescale.

(Bi and Ci) Typical traces obtained in response to 400 ms current steps before (control), immediately after stimulation (stim), and 25 min post-stimulation (25 min PS) in the absence and presence of atropine, respectively. The scale applies to all traces.

(Bii and Cii) Mean action potential numbers (AP. No.) before and after cholinergic afferent stimulation with and without atropine.

(Biii and Ciii) Typical action potentials and phase plane plots before, immediately after, or 25 min post-stimulation when atropine was absent or present.

(Biv and Civ) Individual (open square) and mean (filled squares) spike threshold before and after stimulation without and with atropine.

(Bv) The spike threshold change time course after stimulation in a subset of control neurons.

(Bvi) Representative 50 Hz glutamatergic EPSP trains and alpha EPSPs before and after cholinergic stimulation. Also shown are the average spike numbers produced prior to and post cholinergic stimulation.

(Bvii) Example records and average frequency of spontaneous action potentials before and after HF cholinergic stimulation is shown on the right. In all graphs, the numbers of observations are indicated in parenthesis and asterisks denote significant (p < 0.05) differences.

1992) and hexamethonium (200 μM, a nicotinic receptor antagonist) (Papke et al., 2010) (spike threshold change with nicotinic receptor inhibitors = 5.58 ± 0.5 mV [n = 6]; Table S2). If atropine was applied *following* HF cholinergic fiber stimulation (initial EPSP amplitude = 0.54 ± 0.2 mV [n = 6]; summation ratio = 5.87 ± 0.7), the long-lasting spike threshold decrease and increased granule cell firing still occurred (spike threshold decrease immediately and 25 min post-stimulation = 4.28 ± 0.4 mV and 4.78 ± 0.4 mV [n = 6]; Tables S1 and S2). Thus, muscarinic receptor activation was required for the initiation but not the maintenance of the acetylcholine-mediated spike threshold plasticity.

Further, the muscarinic receptor agonist, oxotremorine-M (Oxo-M; 1 μM) replicated the effects of cholinergic fiber stimulation. Oxo-M enhanced action potential firing and decreased spike threshold, which persisted for up to 40 min following Oxo-M washout (Figures 2A and 2F). However, since Oxo-M was bath applied, it had added global effects on granule cell excitability. Thus, Oxo-M, like neostigmine, produced several epiphenomena: RMP depolarization, enhanced R_N, and an afterdepolarization (ADP) after the action potentials (Figure 2A, Table S2). These ancillary effects fully reversed upon washout and so did not contribute to the persistent increase in spiking induced by Oxo-M.

Muscarinic Receptor-Induced Intrinsic Plasticity Is Axon Dependent

Is the acetylcholine-induced long-lasting spike threshold decrease axonal? To test this, we patched onto neurons situated near the slice surface whose axons were severed, as shown by post hoc morphological analysis (residual axon length = 6.11 ± 1.2 μm, n = 18; referred to as "axonless" neurons; Figure S4). Sholl analysis showed that the dendritic trees of neurons with intact axons and axonless cells were comparable (Sholl, 1953) (Figure S4). The intrinsic membrane properties of neurons with and without an axon were also similar, indicating that the somato-dendritic conductance properties were unchanged by axon cutting (Table S3). Unlike in long axon neurons (Figure 2A), 1 μM Oxo-M application onto axonless neurons did not alter the spike threshold or granule cell firing (Figures 2B and 2F). Oxo-M, though, still depolarized the RMP, enhanced R_N, and induced an ADP following action potential firing in a reversible manner, to an extent comparable to that observed in neurons with axons (Figure 2B, Table S2). This supports the concept that these auxiliary effects are due to changes in somato-dendritic conductances.

To further test whether the effects of acetylcholine were axonal, we focally applied 1 μM Oxo-M for 20 ms onto axons 25–30 μm from the soma or stimulated cholinergic afferents in the CA3a region (i.e., those targeting distal mossy fibers). Both stimuli lowered the spike threshold and enhanced granule cell firing for at least 30 min but did not alter other intrinsic membrane properties (Figures 2C, 2E, and 2F). Synaptic potential-like events, which occurred if the stimulation electrode was placed near proximal dendrites (Figure 1), were not observed either. In contrast, a local puff of 1 μM Oxo-M onto proximal granule cell dendrites 25–30 μm from the soma resulted in a

robust excitatory synaptic potential-like event (amplitude = 5.88 ± 2.2 mV, n = 5), greater than that with proximal dendrite cholinergic fiber stimulation (Figure 1A), but had little effect on action potential threshold (Figures 2D and 2F). Instead, the RMP depolarized, R_N was enhanced, and a small ADP was induced, effects that reversed fully within 10 min of washout (Figure 2D, Table S2). Hence, axonal and somato-dendritic muscarinic receptors have differential effects: somato-dendritic receptor activation leads to synaptic potential-like events, RMP and R_N alterations, and an ADP, while axonal muscarinic receptor stimulation solely causes sustained action potential threshold changes. Since cholinergic fiber stimulation results in a long-lasting spike threshold change only, these data strongly suggest that synaptically released acetylcholine alters granule cell axonal function by preferentially activating axonal muscarinic receptors.

Muscarinic Receptors Are Located on Mossy Fibers, which Cholinergic Axons Contact

To test whether muscarinic receptors are axonal, we performed immunogold labeling using selective M1 and M3 receptor antibodies (Yamasaki et al., 2010). No discernible labeling was observed with the M3 receptor antibody. However, under experimental conditions that did not yield immunolabelling in M1 receptor null tissue (Yamasaki et al., 2010), M1 receptor antibody labeling was detected in granule cell processes, most strongly in dendrites and spines but also along the entire length of mossy fibers (Figure 2G).
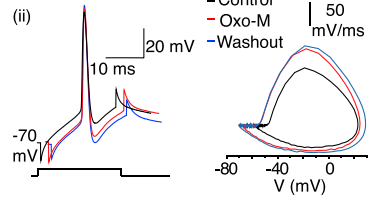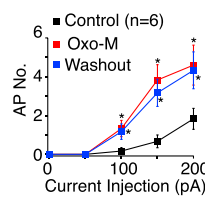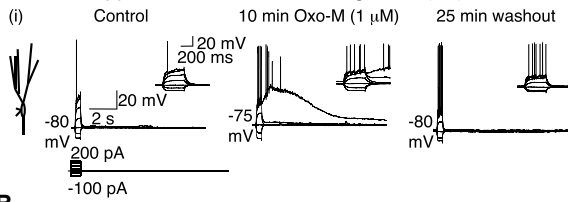
To ascertain whether cholinergic fibers innervate granule cell axons, we performed choline acetyltransferase (ChAT) labeling. This confirmed previous indications (Aznavour et al., 2005) that cholinergic axons are interwoven with mossy fibers (Figure S5). Interestingly, ChAT-immunoreactive fibers and boutons were abundant in close proximity of AISs (identified by β1V spectrin labeling; Figure S5, Movie S1). Thus, local acetylcholine release is likely to activate axonal M1 receptors to induce persistent spike threshold reductions.

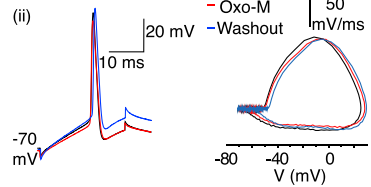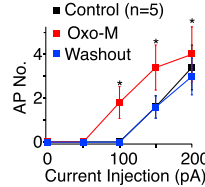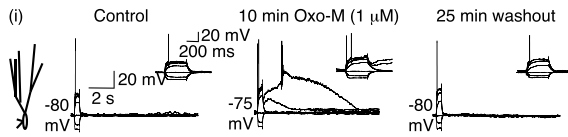### Muscarinic Receptor Activation Does Not Alter AIS Localization or Length

Since action potentials in granule cells initiate at the AIS (Schmidt-Hieber and Bischofberger, 2010), this suggests that AIS properties are altered following muscarinic receptor activation. The effects that we observed could be due to (1) altered AIS position or (2) modified AIS ion channel expression and/or biophysical properties (Grubb and Burrone, 2010).

We first determined whether AIS localization was altered by performing immunohistochemical analysis in control and Oxo-M-treated slices. Electrophysiological recordings before fixation confirmed that Oxo-M caused spike threshold plasticity (Figure 2A). There was no difference in βIV spectrin, Na_V subunits, and ankyrin G labeling between control and Oxo-M-treated slices. The labeling intensity of these peaked ∼10 μm from the soma (Figure S6). The average AIS lengths in control and Oxo-M-treated slices were 28.84 ± 1.05 μm (n = 57, 3 slices) and 26.58 ± 3.14 μm (n = 59, 3 slices, p = 0.54), respectively. This indicates that acute muscarinic receptor activation does not alter the AIS localization or length.
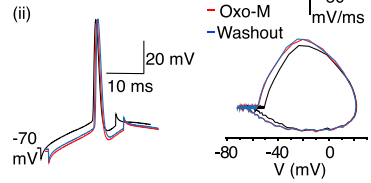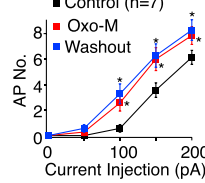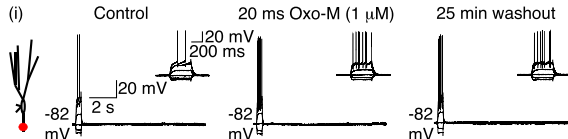
A Global application of Oxo-M to Long Axon (LA) Neurons
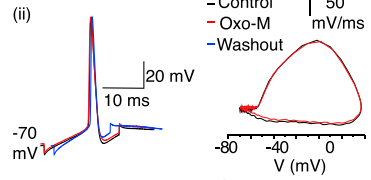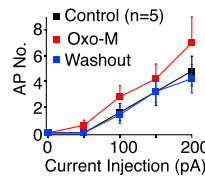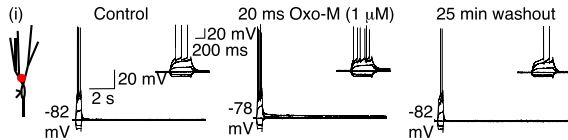
(i) Control   10 min Oxo-M (1 μM)   25 min washout
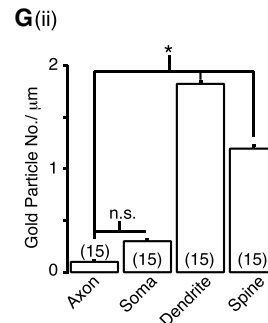
B Global application of Oxo-M to axonless Neurons

(i) Control   10 min Oxo-M (1 μM)   25 min washout

C Local application of Oxo-M onto axons only

(i) Control   20 ms Oxo-M (1 μM)   25 min washout

D Local application of Oxo-M onto dendrites only

(i) Control   20 ms Oxo-M (1 μM)   25 min washout

E Stimulation of cholinergic fibers targeting distal GC axons

(i) Control   Stim   25 min post stim

F **(i)**

AP Threshold (mV)
Control   + Oxo-M   Washout
- LA neurons (n=6)
- Axonless neurons (n=5)
- Local Oxo-M to axons (n=7)
- Local Oxo-M to dendrites (n=5)
- Distal Axon Cholinergic Stimulation (n=5)

F(ii)   Oxo-M (1 μM)

AP Threshold (mV)
Time (min)
- LA neurons (n=5)
- Axonless neurons (n=4)

G **(i)**   Dentate Gyrus   Dentate Gyrus   CA3c

G(ii)

Gold Particle No./ μm
Axon (15)   Soma (15)   Dendrite (15)   Spine (15)
n.s.   *
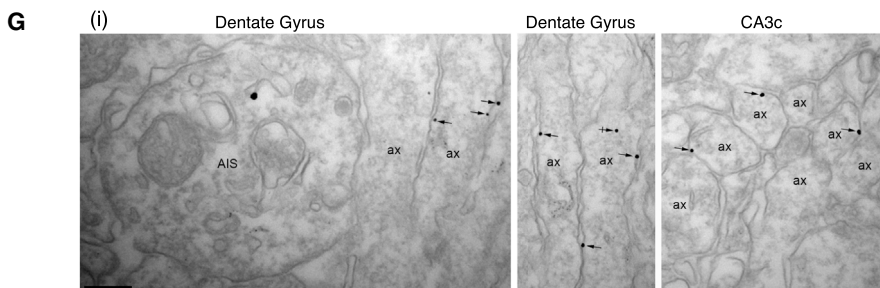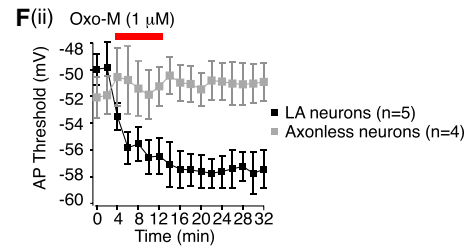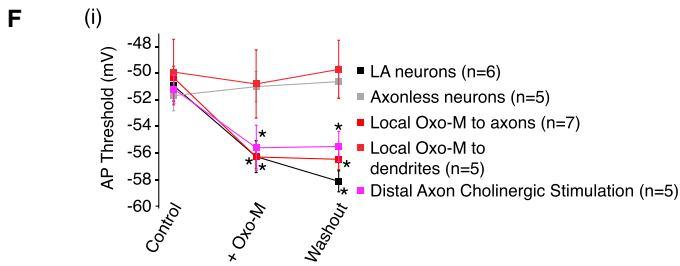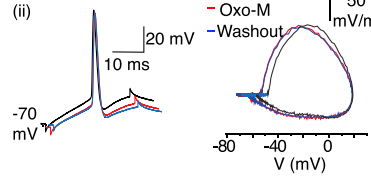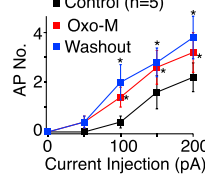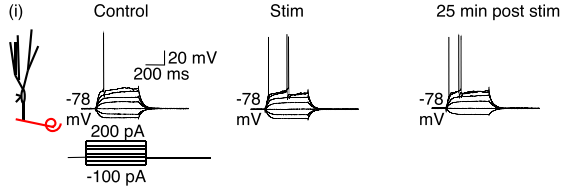
(legend on next page)

Suppressed Axonal K$_V$7 Channel Function Underlies Muscarinic Receptor-Induced Spike Threshold Long-Term Plasticity

Action potential initiation and upstroke in granule cells are dependent upon Na$^+$ channels (Schmidt-Hieber and Bischof-berger, 2010). As the action potential amplitude and width were not altered by endogenous acetylcholine or external application of Oxo-M (Table S1), Na$^+$ channel properties were unlikely to have been affected. In support, the AIS Na$_V$ subunit antibody labeling distribution and intensity in control and Oxo-M-treated slices was similar (Figure S6).

Mossy fibers express K$_V$7, K$_V$7.2 and K$_V$7.3 subunits too (Cooper et al., 2001). K$_V$7 channels underlie a non-inactivating K$^+$ current, the M current (Brown and Passmore, 2009), that is inhibited by muscarinic receptors and regulates the action potential threshold in many central neurons (Battefeld et al., 2014; Shah et al., 2008; Shen et al., 2005). Immunohistochemistry showed that K$_V$7.2 and K$_V$7.3 subunits were located in granule cell distal AIS (approximately 20 μm from the soma; Figure S6). Oxo-M treatment did not affect their expression and distribution (Figure S6).

Do K$_V$7 channels modulate the granule cell spike threshold? Application of the specific K$_V$7 channel inhibitor, XE991 (3 μM; Brown and Passmore, 2009), enhanced action potential firing in granule cells with intact axons but not in axonless cells (Figure 3). This effect was predominantly due to reduced action potential threshold, RMP and R$_N$ being unaffected (Figure 3, Table S4). Similar results were obtained if axonal K$_V$7 channel function was selectively disrupted by intracellular ankyrin G binding peptide (ABP, YIAEGESDTD; 8 mM) (Shah et al., 2008), but not scrambled ABP (TSEYDAEDIG; 8 mM; Figure 3). Additional XE991 application onto neurons dialysed with ABP, but not those containing sABP, had no further effect (Figure 3). These findings together with K$_V$7.2/7.3 antibody labeling (Figure S6) strongly suggest that K$_V$7 channels are present only in granule cell axons and that their axonal location serves to regulate the action potential threshold. In agreement, we found that the K$_V$7 current measured using voltage clamp could be recorded solely from neurons with long axons but not from axonless neurons (Figure S7).

To discern whether altered K$_V$7 channel function underlies the muscarinic receptor activation-induced persistent action potential threshold reduction, we pretreated granule cells with XE991 (3 μM) and applied either HF cholinergic afferent stimulation or Oxo-M. Neurons treated with XE991 had a lower spike threshold and enhanced excitability than non-treated neurons (Figure 4).

For HF stimulation, the initial EPSP amplitude (0.44 ± 0.1 mV, n = 5) and summation ratio (3.04 ± 1.3 mV, n = 5) were comparable to that in non-XE991-treated neurons. However, neither HF cholinergic afferent stimulation nor Oxo-M application in the presence of XE991 altered the spike threshold or granule cell firing (Figure 4A). Oxo-M subsidiary effects (RMP and R$_N$ changes and ADP induction) still occurred and recovered within 25 min of washout (Figure 4A, Table S2), further supporting the notion that K$_V$7 channels do not underlie these somato-dendritic effects in granule cells.

The above results suggest that axonal K$_V$7 channels are inhibited in a long-lasting manner by brief muscarinic receptor activation. Indeed, a 10 min Oxo-M application abolished the K$_V$7 current, an effect that did not reverse with washout for at least 20 min (Figure 4B). Subsequent application of XE991 had no further effect (Figure 4B). Hence, muscarinic receptor activation induces long-lasting spike threshold plasticity by persistently inhibiting the axonal K$_V$7 current.

The Spike Threshold Plasticity Is Ca^{2+} Dependent

The persistent effect of muscarinic receptor activation on axonal K$_V$7 currents (Figure 4B) was unexpected as cholinergic suppression of the somatic K$_V$7 current in other neurons is fully reversible. It is typically due to membrane phosphatidylinositol-4.5-bisphosphate (PIP$_2$) level depletion (Brown and Passmore, 2009; Gamper and Shapiro, 2007; Shen et al., 2005). Upon cholinergic agonist washout, PIP$_2$ levels are replenished, leading to K$_V$7 current recovery (Brown and Passmore, 2009; Gamper and Shapiro, 2007). Our results imply that PIP$_2$ levels may not recover rapidly at the AIS, leading to prolonged axonal K$_V$7 channel inhibition. To test this, we incorporated the water-soluble analog dioctanoyl (diC8)-PIP$_2$ (125 μM [Lukacs et al., 2013]) in the patch pipette to boost PIP$_2$ levels. Interestingly, Oxo-M still persistently lowered the spike threshold (Figure 5A). The Oxo-M-induced ADP, though, was reduced considerably with diC8-PIP$_2$ (Figure 5A, Table S2), suggesting that somato-dendritic PIP$_2$ levels were increased. It should be noted, though, that the AIS is effectively a surface diffusion barrier (Leterrier and Dargent, 2014) and, therefore, artificially altering PIP$_2$ levels might not affect intrinsic AIS lipid levels. Nonetheless, it suggests that the signaling mechanisms underlying muscarinic-receptor suppression of axonal K$_V$7 currents may differ from that described at neuronal somata.

Intracellular Ca^{2+} ([Ca^{2+}]$_i$) can also suppress the K$_V$7 current (Gamper and Shapiro, 2007; Selyanko and Brown, 1996). Muscarinic receptor stimulation in hippocampal neurons might

---

Figure 2. The Muscarinic Receptor-Induced Action Potential Threshold Long-Term Plasticity Is Axon Dependent

(Ai, Bi, Ci, Di, and Ei) Representative traces under control conditions, after either global or local application of Oxo-M (1 μM) or stimulation of cholinergic fibers targeting distal granule cell (GC) axons and following 25 min Oxo-M washout or post-stimulation in intact axon (long axon [LA]) neurons or axonless neurons. The RMP is indicated adjacent to the traces. The inset shows the first trace segment on an expanded timescale. The average action potential number (AP No.) under the different conditions is shown on the right. The scales apply to all traces within the panels.

(Aii, Bii, Cii, Dii, and Eii) Typical single action potentials and phase plane plots under control conditions (black), after Oxo-M application or cholinergic fiber stimulation (red) and 25 min following Oxo-M washout or termination of the stimulation paradigm (blue).

(Fi) The mean spike threshold before, during, and 25 min after either Oxo-M treatment or cholinergic afferent stimulation.

(Fii) The threshold change time course during Oxo-M treatment and following washout of Oxo-M.

(Gi) Example electron micrographs showing immunoreactivity for muscarinic M1 receptor subunit. ax, axon; den, dendrites; AIS, axon initial segment. Scale bars, 0.2 μm.

(Gii) Quantification of gold particles labeling M1 receptor subunits in dentate gyrus. The numbers of observations are in parenthesis. n.s., nonsignificant.

A Long Axon (LA) neurons + XE991

(i) Control +XE991

(ii)

B
- LA neurons (n=10)
- LA neurons + XE991
- Axonless cells (n=8)
- Axonless cells + XE991

C Axonless neurons + XE991

(i) Control +XE991

(ii)

D
- LA neuron (n=10)
- Axonless neuron (n=8)

E ABP (YIAEGESDTD)

(i) 2 min 25 min +XE991 (ii)

F sABP (TSEYDAEDIG)

(i) 2 min 25 min +XE991 (ii)

G(i) ABP

G(ii) sABP

H(i)
- ABP (n=6)
- sABP (n=8)

H(ii)
- ABP (n=6)
- sABP (n=8)
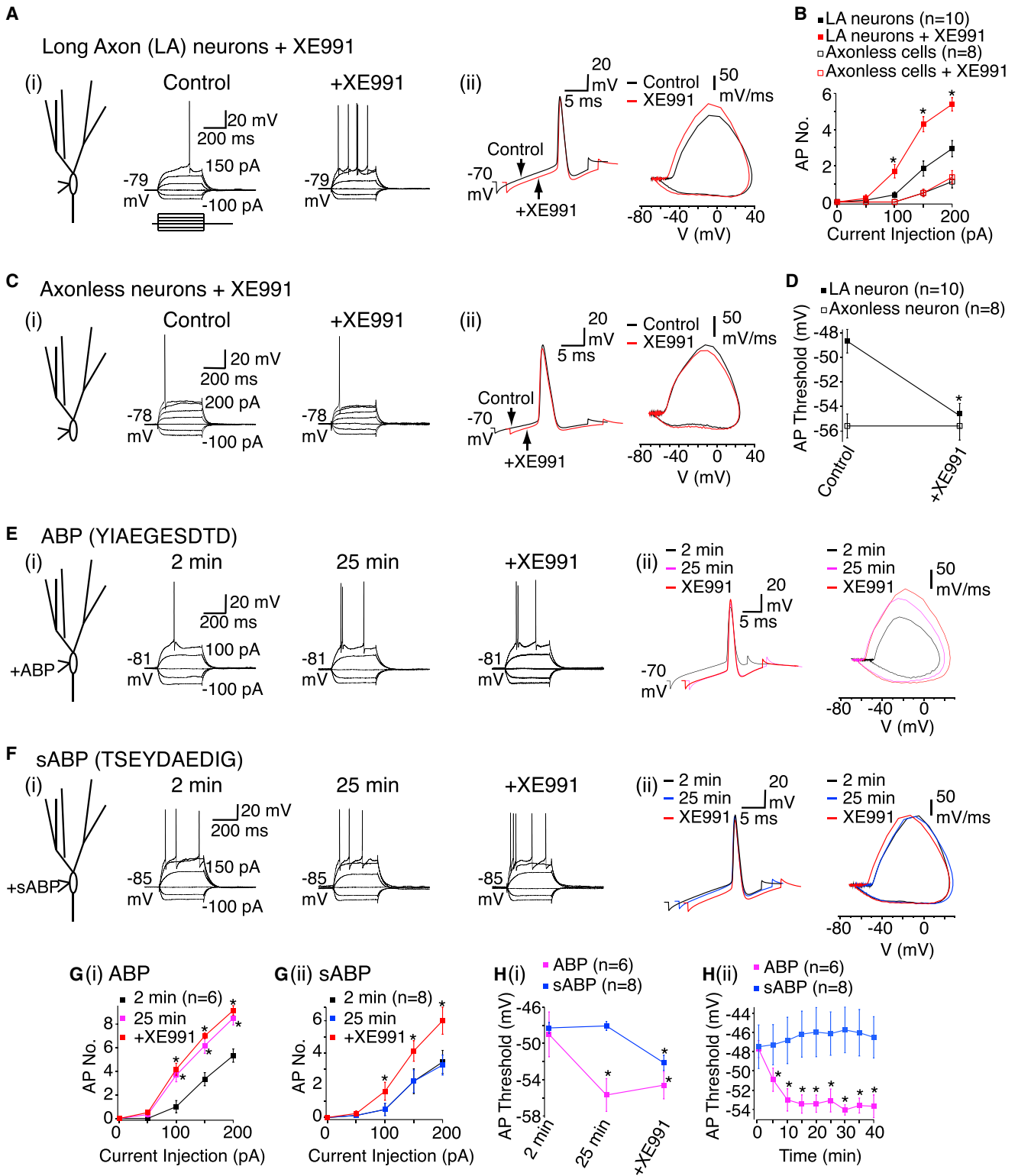
Figure 3. Axonal K$_V$7 Channels Regulate the Action Potential Threshold

(Ai and Ci) Example records from long axon (LA) and axonless granule cells in the absence and presence of XE991 (3 μM). The RMP values are adjacent to the traces. The scale shown applies to both traces in the panel.

(Aii and Cii) Typical spikes and phase plane plots before (black) and after (red) XE991 treatment in LA and axonless neurons.

(legend continued on next page)

raise $[Ca^{2+}]_i$ by Ca^{2+} release from intracellular stores (Gamper and Shapiro, 2007) or augmenting voltage-gated Ca^{2+} channel (VGCC) opening (Park and Spruston, 2012). We tested these possibilities by incorporating 20 mM BAPTA into the patch pipette or applying the VGCC inhibitor, cadmium chloride ($CdCl_2$; 200 μM). Oxo-M treatment then no longer persistently altered the action potential firing or threshold (Figure 5B). Secondary alterations in RMP and R_N still occurred (Figure 5B, Table S2), though the Oxo-M-induced ADP was abolished (Table S2). Hence, muscarinic receptor stimulation elevates $[Ca^{2+}]_i$, via VGCCs to cause spike threshold changes.

Ca²⁺ Entry via T-Type Ca²⁺ Channels Is Required for the Muscarinic Receptor-Induced Effects

Since the spike threshold effects occur at rest (Figure 1B), the VGCCs involved are likely to be low-threshold channels such as T-, R-, and L-type Ca^{2+} channels (Catterall, 2011). Interestingly, in CA1 neurons, muscarinic receptor stimulation enhances R-type Ca^{2+} channel activity (Park and Spruston, 2012). In granule cells, though, the T-type Ca^{2+} channel inhibitors, $NiCl_2$ (50 μM) and TTA-P2 (500 nM) (Dreyfus et al., 2010), but not the R-and L-type Ca^{2+} channel inhibitors, SNX482 (500 nM) and nifedipine (10 μM), prevented the Oxo-M-induced sustained action potential firing and threshold change (Figure 6). All auxiliary effects of Oxo-M (depolarized RMP, enhanced R_N, and ADP generation) still occurred, leading to a reversible increase in action potential firing (Figure 6A, Table S2). TTA-P2 also prevented the effects of HF cholinergic afferent stimulation on granule cell excitability (Figure 6, Table S2) but had little effect on cholinergic EPSP amplitude or summation (summation ratio = 2.50 ± 0.36, n = 5).

The above results suggest that the persistent effects of muscarinic activation on granule cell axons required Ca^{2+} entry via T-type Ca^{2+} channels. Accordingly, Oxo-M effects on the K_V7 current recorded from long axon granule cells were prevented by TTA-P2 (500 nM; Figure 6D). TTA-P2 itself did not affect the K_V7 current and the current was still blocked by 3 μM XE991.

The Spike Threshold Plasticity Is due to Sustained Elevated Axonal Basal Ca²⁺ Entry via T-Type Ca²⁺ Channels

We next asked whether T-type Ca^{2+} channels are present in mossy fibers. Three subunits, $Ca_V3.1$–3.3, encode for T-type Ca^{2+} channels (Catterall, 2011). $Ca_V3.2$ antibody immunogold particles were detected on wild-type axons, dendrites, and somata spines (Figure 7A). The granule cell axon $Ca_V3.2$ labeling, although less than in dendrites and spines, was significantly greater than that in $Ca_V3.2$ null granule cell axons (Figure 7A), indicating that $Ca_V3.2$ subunits are located in mossy fibers.

Do muscarinic receptors activate axonal T-type Ca^{2+} channels? To test this, we imaged Ca^{2+} in granule cell axons using two-photon microscopy. Oxo-M application depolarized somata by 6.29 ± 0.7 mV (n = 8). Simultaneously, the axonal basal $[Ca^{2+}]_i$ was increased significantly (Figure 7B). Interestingly, the axonal basal $[Ca^{2+}]_i$ augmentation only partly recovered following washout of Oxo-M for up to 40 min and reached a new baseline level significantly above the control, despite the RMP fully recovering (Figure 7B). The axonal $[Ca^{2+}]_i$ increase was not due to a somatic RMP change because a 6 mV somatic depolarization caused a substantially smaller axonal $[Ca^{2+}]_i$ rise than that observed with Oxo-M and fully reversed on RMP restoration (data not shown). The Oxo-M-induced basal axonal $[Ca^{2+}]_i$ escalation was abolished by TTA-P2 (500 nM; Figure 7B). Hence, muscarinic receptor activation increases basal T-type Ca^{2+} channel function in granule cells resulting in a long-term rise in basal axonal $[Ca^{2+}]_i$.

Previous studies have indicated that axonal T-type Ca^{2+} currents can regulate the action potential threshold (Bender et al., 2010; Ohkuma et al., 2013). T-type Ca^{2+} channel inhibitors, though, did not affect the granule cell spike threshold (Figure 6B). In support, we found the action potential-associated $[Ca^{2+}]_i$ rise was similar under control conditions, following 10 min Oxo-M treatment and after 25 min washout (Figure 7C). This reinforces the notion that Oxo-M-augmented T-type Ca^{2+} channel activity predominantly enhances basal axonal $[Ca^{2+}]_i$ levels.

One reason might be that the biophysical properties of axonal T-type Ca^{2+} channels are altered. We thus recorded the T-type Ca^{2+} current from long axon and axonless neuronal somata. T-type Ca^{2+} currents were stable for up to 40 min, activated above −80 mV (Figure S8), and were inhibited by TTA-P2 (500 nM, n = 16) and $CdCl_2$ (200 μM, n = 3) but not XE991 (3 μM, n = 6; data not shown). Although the half-activation potentials in long axon ($V_{1/2}$ = −61.2 ± 1.3 mV, n = 8) and axonless ($V_{1/2}$ = −59.6 ± 1.4 mV, n = 6) neurons were comparable, the current amplitudes were significantly smaller in axonless neurons than long axon neurons (maximal amplitude at −40 mV in long axon and axonless neurons = 112.5 ± 11.0 pA [n = 8] and 70.7 ± 18.8 pA [n = 6], p < 0.05). Oxo-M shifted the T-type Ca^{2+} current activation curve in long axon neurons, but not axonless neurons, to the left without affecting the slope of the curve (Figure S8). The currents at −80 mV and −70 mV were substantially enhanced by Oxo-M in long axon neurons but the peak current amplitudes were no different (Figure S8). These Oxo-M effects on T-type Ca^{2+} currents in long axon neurons were maintained for at least 25 min following washout (Figure S8). Hence, these results strongly support the idea that muscarinic receptor

(B and D) Average spike numbers (AP No.) in response to 400 ms current pulses and mean spike threshold under control conditions and following XE991 treatment in LA and axonless neurons, respectively.

(Ei and Fi) Representative traces and RMP values (adjacent to the traces) when either ABP (8 mM) or scrambled ABP (sABP, 8 mM) were included in the patch pipette for 2 min (control) and 25 min. XE991 was subsequently applied. The scale shown applies to all traces in the panel.

(Eii and Fii) Action potentials at 2 min, 25 min, and after XE991 treatment when ABP and sABP were incorporated in the intracellular solution, respectively.

(G and Gii) Average spike numbers generated with varying 400 ms current pulses 2 min and 25 min after ABP/sABP dialysis and following XE991 treatment.

(Hi) Average spike threshold 2 min, 25 min, and after XE991 with ABP or sABP.

(Hii) The action potential threshold time course with ABP or sABP.

A In the presence of XE991 (3 μM)
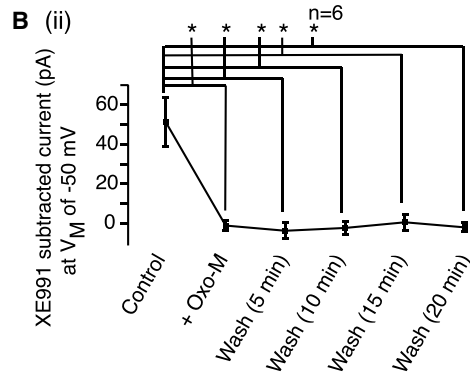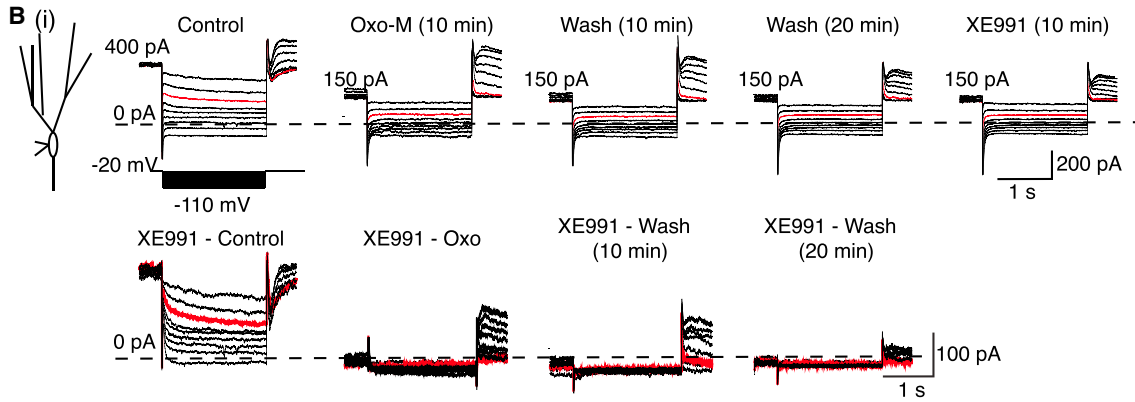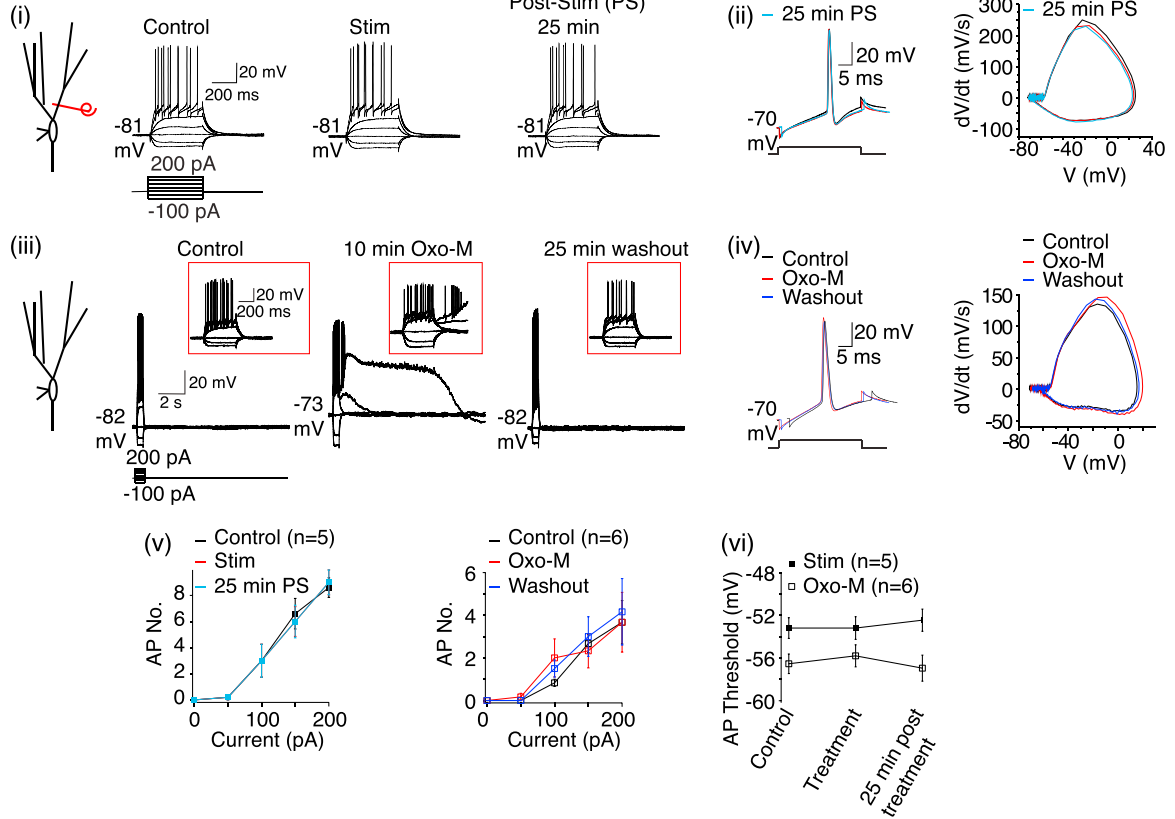
(legend on next page)

activation leads to a persistent rise in axonal basal $[Ca^{2+}]_i$ by enhancing T-type Ca^{2+} channel function.

T-Type Ca^{2+} Channel Inhibition Fully Reverses the Spike Threshold Plasticity

If the persistent increase in T-type Ca^{2+} channel activity at rest is the cause of the muscarinic receptor-induced action potential threshold plasticity, then applying TTA-P2 *after* Oxo-M should rescue this. Indeed, we found that inclusion of TTA-P2 (500 nM) during washout after Oxo-M treatment of granule cells restored the spike firing and threshold to that observed under control conditions (Figure 8).

Moreover, since T-type Ca^{2+} channels are not active at −90 mV (Figure S8), muscarinic receptor activation at this potential would not be predicted to induce action potential threshold or firing alterations. In support, 1 μM Oxo-M application and washout had little effect on spike threshold or firing at −90 mV (control and Oxo-M spike threshold difference = 0.55 ± 0.4 mV [n = 6]). Hence, our findings strongly suggest that muscarinic receptor activation in granule cells leads to a long-term enhanced T-type Ca^{2+} channel openings at rest, which results in sustained elevated $[Ca^{2+}]_i$ and persistently reduced axonal K_V7 channel function.

DISCUSSION

We found that synaptically released acetylcholine preferentially lowered the action potential threshold in granule cells, an effect that persisted at least 30 min (Figure 1, Figures S1–S3). Consequently, there was a greater propensity for granule cells to elicit action potentials with depolarizing stimuli and E-S coupling and spontaneous spike frequency were enhanced (Figure 1). These effects were due to axonal muscarinic receptor-induced sustained enhancement of axonal T-type Ca^{2+} channel function at rest (Figures 2, 6, and 7, Figure S8) such that axonal basal $[Ca^{2+}]_i$ was elevated (Figure 7). This inhibited K_V7 channel function (Figure 5), and as K_V7 channels regulate the spike threshold in granule cells (Figure 3), there was a prolonged reduction in this. Indeed, the long-lasting decrease in spike threshold could be reversed if T-type Ca^{2+} channel activity was inhibited following the muscarinic receptor stimulation (Figure 8). Given that increased granule cell spike frequency will result in more effective discharge of post-synaptic hippocampal CA3 neurons (Henze et al., 2002), our results suggest that acetylcholine is likely to boost granule cell information processing by augmenting axonal signaling. As granule cell activity is normally sparse in vivo (Henze et al., 2002; Pernía-Andrade and Jonas, 2014),

this is likely to be a critical mechanism for enhancing their excitability to allow efficient information transfer to post-synaptic neurons.

Cholinergic Afferent Stimulation Preferentially Modulates Axonal Excitability in Granule Cells

ChAT labeling showed that cholinergic fibers project to DG molecular, granular, and hilus regions where granule cell dendrites, somata, and axons are located (Figure S5) (Aznavour et al., 2005). Remarkably, in these neurons electrical or optical stimulation paradigms, with or without glutamate and GABA receptor inhibitors, resulted in endogenous acetylcholine release that affected the action potential threshold only (Figure 1, Figures S1 and S2). Other spike characteristics or intrinsic membrane properties were unaltered. This suggested that the acetylcholine effects were axonal. In support, Oxo-M local axonal application or cholinergic afferent stimulation to axons replicated these findings (Figure 2). Muscarinic receptors were located on mossy fibers but their density was lower than in dendrites and spines (Figure 2G). These findings suggest that the effects of endogenous acetylcholine release are highly specific and constrained to defined targets and cholinergic fiber stimulation preferentially activates axonal muscarinic receptors, even though they are present at a lower density in axons. This is in line with previous studies using cell lines that show that a small fraction of receptors adequately causes the appropriate downstream effects (Falkenburger et al., 2013).

One reason for the preferential axonal response might be that granule cell dendritic intrinsic properties are such that signals received by these are strongly attenuated (Krueppel et al., 2011). Synaptically released acetylcholine may have also stimulated dendritic muscarinic receptors because this, like focal application of Oxo-M to dendrites, produced synaptic potential-like events (Figure 1). This dendritic muscarinic receptor activation, though, was not sufficient to cause intrinsic membrane property alterations that are associated with somato-dendritic receptor activation (Figure 2). Nonetheless, under some conditions, cholinergic afferent inputs might robustly activate dendritic muscarinic receptors, leading to altered somato-dendritic membrane properties, as in hippocampal pyramidal neurons (Buchanan et al., 2010; Cole and Nicoll, 1983; Gu and Yakel, 2011). Indeed, in the presence of neostigmine, a significantly greater reduction in spike threshold together with a transient somatic RMP depolarization occurred (Figure S3). The RMP depolarization is likely to be due to increased somato-dendritic muscarinic receptor recruitment from enhanced volume transmission of synaptically released acetylcholine. This indicates that the


Figure 4. Suppressed K_V7 Currents Underlie Muscarinic Receptor-Mediated Spike Threshold Decrease

(Ai and Aiii) Typical responses from neurons pre-treated with XE991 under control conditions, after HF stimulation or treatment with Oxo-M for 10 min and 25 min following stimulation or washout of Oxo-M. The insets in (Aiii) show the first 1 s of the trace on an expanded timescale. The scales apply to all traces.

(Aii and Aiv) Example single action potentials and phase plane plots before, after treatment (high-frequency stimulation or Oxo-M), and 25 min post-treatment.

(Av and Avi) Average action potential numbers (AP No.) and action potential threshold generated in pre-treated XE991 neurons before, during, and 25 min after high-frequency stimulation or Oxo-M treatment.

(Bi) Raw current traces obtained when the de-activation protocol was applied under control conditions, after 10 min 1 μM Oxo-M, washout, and after XE991 application. The records in the presence of XE991 were subtracted from those in the absence to obtain the XE991-subtracted K_V7/M currents (traces obtained with hyperpolarization to −50 mV in red). The scales apply to all traces.

(Bii) The average XE991-subtracted current at −50 mV prior to, during Oxo-M, and after 5–20 min Oxo-M washout.
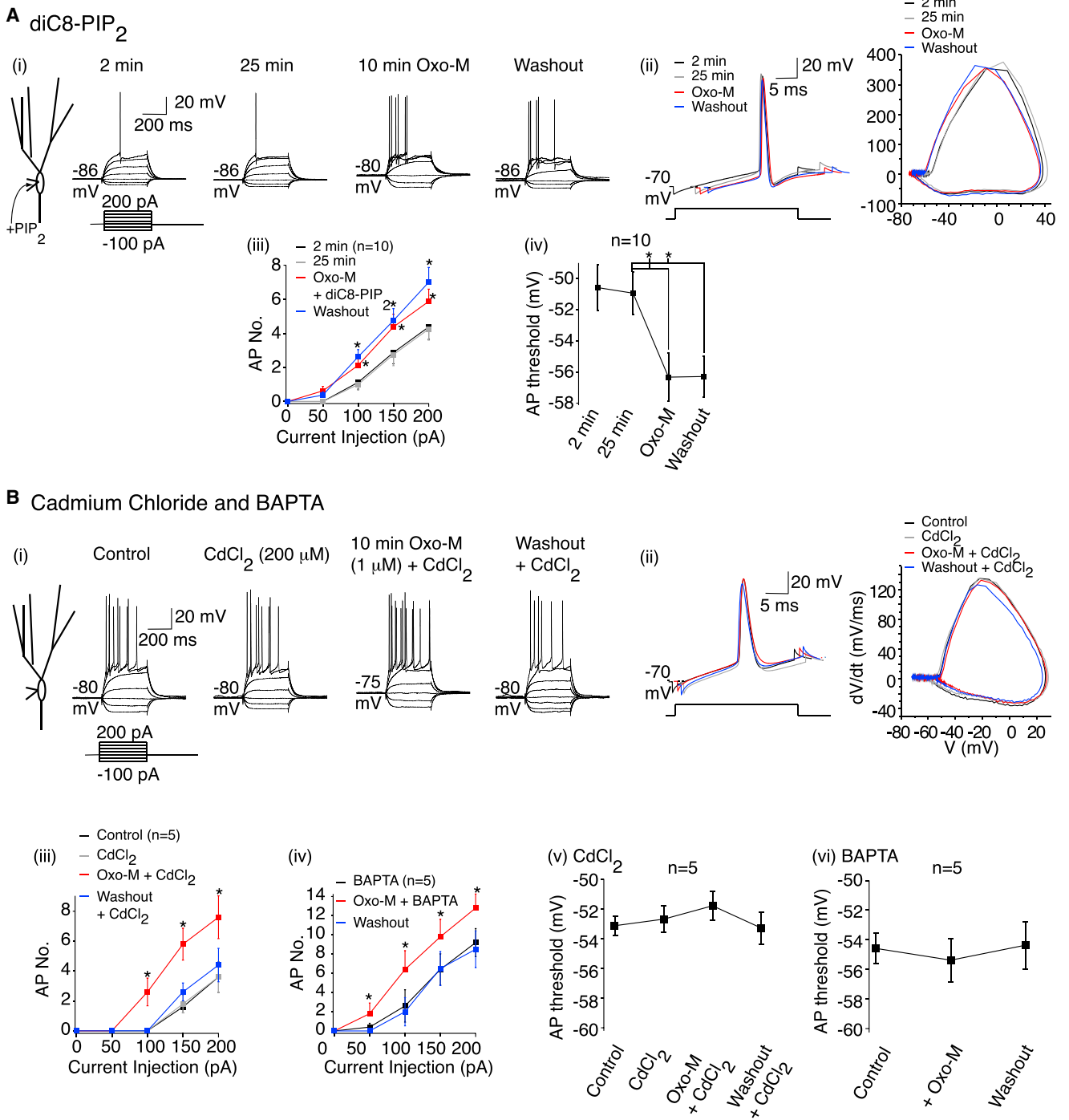
Figure 5. Muscarinic Receptor-Induced Spike Threshold Long-Lasting Plasticity Is Calcium Dependent

(Ai and Bi) Example traces showing the effects of diC8-PIP$_2$ (125 μM) and cadmium chloride (CdCl$_2$; 200 μM) in the absence and presence of Oxo-M (1 μM). diC8-PIP$_2$ controls were obtained 2 min after achieving whole cell. The RMP values are indicated adjacent to the traces. The scales apply to all traces.

(Aii and Bii) Typical action potentials and associated phase plane plots when diC8-PIP$_2$ was included in the patch pipette or CdCl$_2$ applied.

(Aiii, Aiv, Biii, Biv, Bv, and Bvi) The average action potential number (AP No.) and mean spike threshold values before, during, and after Oxo-M treatment when diC8-PIP$_2$ or BAPTA (20 mM) was included in the patch pipette or CdCl$_2$ applied.

cholinergic fiber stimulation strength coupled, perhaps, with the pattern of stimulation in vivo might dictate axonal versus dendritic effects of acetylcholine.

The preferential axonal function alteration by cholinergic afferent stimulation is of considerable significance for granule cells. Most glutamatergic synaptic inputs are onto granule cell dendrites but, as dendritic signals in granule cells are significantly attenuated, only strong inputs will impact their excitability (Krueppel et al., 2011). Our results suggest that the cholinergic fiber stimulation dynamically boosts granule cell activity so that even weak synaptic information received by their dendrites can be efficiently transferred to post-synaptic neurons. Indeed, E-S potentiation and spontaneous action potential frequency were enhanced following cholinergic afferent stimulation (Figure 1B). Consequently, mossy fiber transmission may be enhanced, leading to enhanced synaptic potentiation at these synapses.

Enhanced T-Type Ca^{2+} Channel Activity Underlies the Axonal Muscarinic Receptor-Induced Effects

We show that that muscarinic receptor stimulation led to a persistent axonal basal [Ca^{2+}]$_i$ enhancement by increasing T- (Ca$_V$3.2) type Ca^{2+} channel activity at rest (Figures 6 and 7). This was due to a shift in the axonal T-type Ca^{2+} activation curve by muscarinic receptors (Figure S8). As Ca$_V$3.2 subunits are expressed globally in granule cells (Figure 7), this suggests that the coupling of muscarinic receptors to Ca$_V$3.2 channels might be weaker in somata and dendrites compared with axons. Accordingly, Oxo-M did not alter somato-dendritic T-type currents in axonless neurons (Figure S8). Although this was unexpected, a selective axonal, but not dendritic, T-type Ca^{2+} channel inhibition by dopamine occurs in cochlear interneurons (Bender et al., 2010). Hence, axonal signaling microdomains might differ from those in other neuronal compartments.

Cholinergic receptor-induced T-type Ca^{2+} channel activation is both necessary and sufficient for the enhanced excitability as T-type Ca^{2+} channel antagonists prevented and reversed the spike threshold long-lasting plasticity (Figures 6 and 8). Unlike in some other neurons (Bender et al., 2010; Ohkuma et al., 2013), the T-type Ca^{2+} channels per se did not affect the action potential threshold (Figure 6). Further, though T-type Ca^{2+} channel activity at potentials near the granule cell RMP were enhanced by Oxo-M, the current at voltages near the spike threshold were similar (Figure S8). In support, the spike-associated [Ca^{2+}]$_i$ rise was similar before and after Oxo-M treatment (Figure 7). The axonal basal [Ca^{2+}]$_i$ rise by Oxo-M then suppressed axonal K$_V$7 current, which regulates the spike threshold (Figures 3 and 5) While it is known that [Ca^{2+}]$_i$ ≤ 100 nM inhibits K$_V$7/M channels (Selyanko and Brown, 1996), the muscarinic receptor-induced sustained Ca^{2+} entry via T-type Ca^{2+} channels causing K$_V$7 channel plasticity is a novel, distinct phenomenon.

How might brief muscarinic receptor activation lead to a persistent shift in T-type Ca^{2+} activation curve (Figure S8)? Native and expressed Ca$_V$3.2 currents (including those in some interneuron AISs [Bender et al., 2010]) are modified by kinases such as protein kinase C (Bender et al., 2010; Park et al., 2006). Since muscarinic receptor stimulation alters the activity of multiple kinases, there is a strong possibility that the musca-

rinic receptor-induced axonal T-type Ca^{2+} channel long-term plasticity is kinase mediated too.

In summary, our findings show that cholinergic fiber activation reduces the action potential threshold persistently such that granule cells will respond with greater fidelity to additional excitatory inputs (Figure 1). This is, as yet, an unreported action of acetylcholine that might influence cognitive function. While, we conducted our study in the dentate gyrus, the findings may also be applicable to other hippocampal regions. In fact, cholinergic fibers innervate the stratum oriens where hippocampal CA1 and CA3 neuron axons reside (Aznavour et al., 2005). In these neurons, K$_V$7 subunits are axonal (Devaux et al., 2004) and also play a significant role in setting the action potential threshold (Shah et al., 2008). Hence, the acetylcholine-induced action potential threshold long-lasting plasticity might be a common cellular mechanism that plays a fundamental role in neuronal information processing and storage.

EXPERIMENTAL PROCEDURES

Acute Slice Preparation

The UK Home Office approved all procedures. 22- to 27-day-old male Sprague Dawley rat pups and 5- to 6-week-old B6 mice expressing channelrhodopsin 2 (ChR2) and eYFP in cholinergic fibers (kind gift from Prof. D. Kullman, UCL Institute of Neurology) were decapitated and the brain removed and submerged in ice-cold solution containing the following: 87 mM NaCl, 25 mM NaHCO$_3$, 10 mM glucose, 75 mM sucrose, 2.5 mM KCl, 1.25 mM NaH$_2$PO$_4$, 0.5 mM CaCl$_2$, 7 mM MgCl$_2$ (pH 7.3), 325 mOsm/l. The brain was hemi-sected and a cut parallel to the dorsal part of the brain made. The ventral side brain halves were glued onto a slice holder and 350 μm slices made (Leica VT1200S, Leica). Slices were incubated in the cutting solution for 10 min at 35°C and then stored at room temperature.
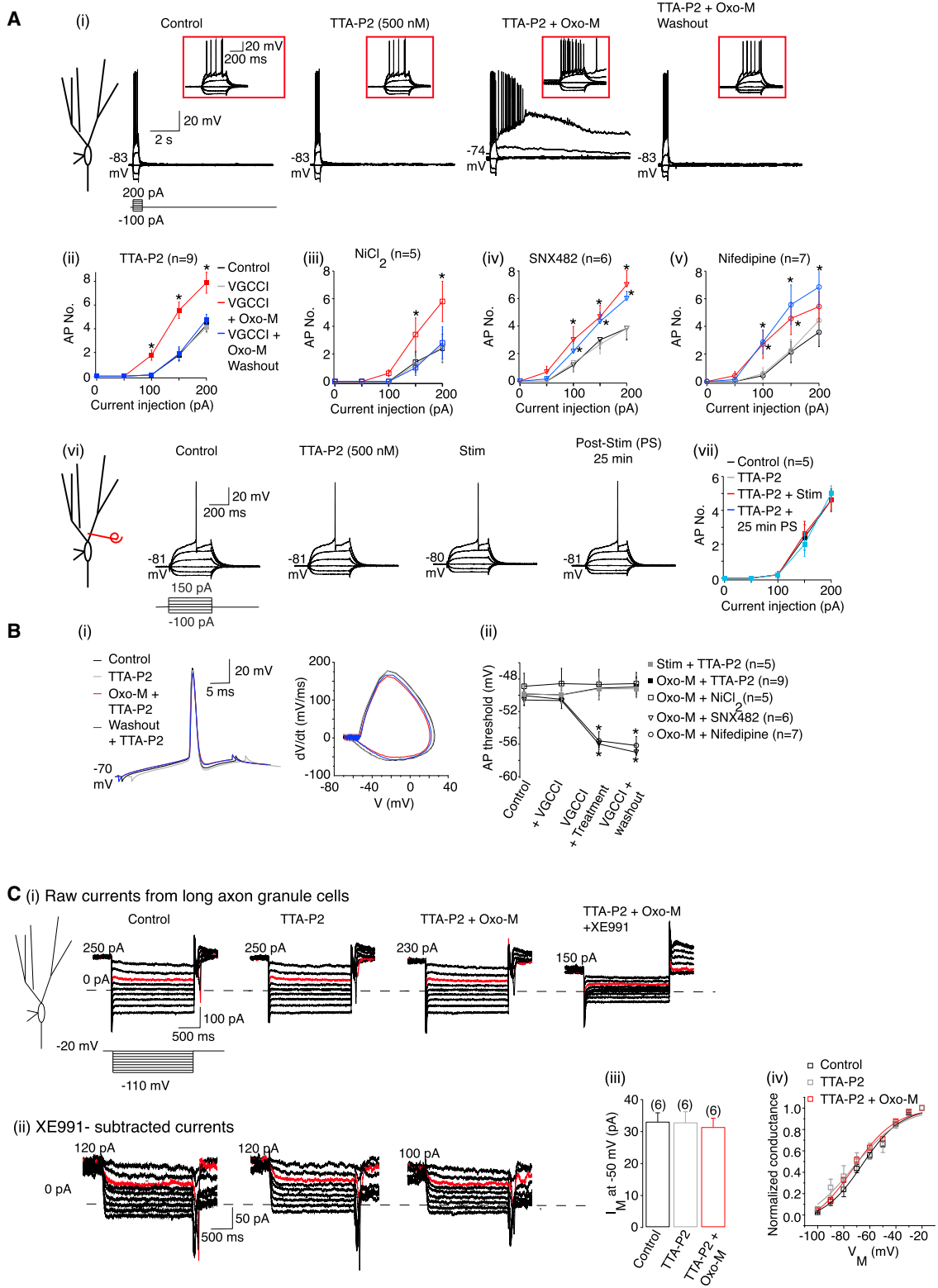
Electrophysiological Whole-Cell Recordings

Slices were transferred to a submerged chamber containing external solution containing the following: 125 mM NaCl, 25 mM NaHCO$_3$, 25 mM glucose, 2.5 mM KCl, 1.25 mM NaH$_2$PO$_4$, 2 mM CaCl$_2$, 1 mM MgCl$_2$, 0.05 mM CNQX, 0.05 mM DL-AP5, 0.01 mM bicuculline, 0.001 mM CGP 55845 (pH 7.3), 32°C–36°C. The internal pipette solution contained the following: 120 mM KMeSO$_4$, 15 mM KCl, 10 mM HEPES, 2 mM MgCl2, 0.2 mM EGTA, 2 mM Na$_2$ATP, 0.3 mM Tris-GTP, and 14 mM Tris-phosphocreatinine (pH 7.3) with KOH, 295–300 mOsm/l. In some experiments, 8 mM ABP or sABP was added to the internal solution. When 20 mM K$_4$BAPTA was added to the pipette solution, KMeSO$_4$ was reduced to 60 mM and osmolarity adjusted by adding N-methyl-d-glucamine (NMDG). Pipettes had resistances of 5–8 MΩ. In all experiments, Neurobiotin (0.2% w/v) was included in the intracellular pipette solution. Slices were fixed in 4% paraformaldehyde and stained with streptavidin Alexa Fluor 488 conjugate 24 hr later (Huang et al., 2012)

Electrophysiological recordings were made using a Multiclamp 700B amplifier (Molecular Devices). Recordings were filtered at 10 kHz and sampled at 50 kHz. Data were acquired using pClamp 10.0 (Molecular Devices). Series resistance was in the order of 10–20 MΩ. Recordings were discarded if the series resistance increased by more than 20%.

All reagents were purchased from Sigma-Aldrich apart from tetrodotoxin, bicuculline, CGP 55845, DL-AP5, and XE991, which were obtained from Abcam. Neurobiotin was acquired from Vector Laboratories and streptavidin Alexa Fluor 488 was procured from Life Technologies.

Cholinergic Afferent Stimulation Experiments

Unless otherwise stated, the following was added to the whole-cell external recording solution: 0.1 mM (RS)-α-Methylserine-O-phosphate (MSOP) and 1 mM (RS)-α-Methyl-4-carboxyphenylglycine (MCPG) disodium salt. Cholinergic afferents were electrically stimulated using tungsten electrodes (A-M systems) or by activating channelrhodopsin with a 488 nm laser (Cairn

A (i)

Control TTA-P2 (500 nM) TTA-P2 + Oxo-M TTA-P2 + Oxo-M Washout

(ii) TTA-P2 (n=9)
— Control
— VGCCI
— VGCCI + Oxo-M
— VGCCI + Oxo-M Washout

(iii) NiCl$_2$ (n=5)

(iv) SNX482 (n=6)

(v) Nifedipine (n=7)

(vi) Control TTA-P2 (500 nM) Stim Post-Stim (PS) 25 min

(vii)
— Control (n=5)
— TTA-P2
— TTA-P2 + Stim
— TTA-P2 + 25 min PS

B (i)
— Control
— TTA-P2
— Oxo-M + TTA-P2
— Washout + TTA-P2

(ii)
■ Stim + TTA-P2 (n=5)
■ Oxo-M + TTA-P2 (n=9)
□ Oxo-M + NiCl$_2$ (n=5)
▽ Oxo-M + SNX482 (n=6)
○ Oxo-M + Nifedipine (n=7)

C (i) Raw currents from long axon granule cells

Control TTA-P2 TTA-P2 + Oxo-M TTA-P2 + Oxo-M +XE991

(ii) XE991- subtracted currents

(iii)

(iv)
□ Control
□ TTA-P2
□ TTA-P2 + Oxo-M

(legend on next page)

Research). 8–10, 0.1 ms, 50–200 μA pulses or 8, 10 ms, 9 mW light pulses were delivered.

E-S Coupling Experiments

CNQX and APV were omitted from the external solution. Glutamatergic EPSPs were evoked using tungsten electrodes placed in stratum moleculare 100–150 μm from granule cell bodies. 10, 0.1 ms pulses were applied at 50 Hz. Simulated EPSPs were generated by injecting the waveform:

$$A = (t/\tau)^* \exp(1 - (t/\tau))$$

where A is the injected current amplitude and τ is the rise time constant.

Spontaneous Action Potential Recordings

"Loose" seals of 236.8 ± 52 MΩ were made with 3–5 MΩ patch pipettes filled with 150 mM NaCl. The external solution lacked glutamate receptor blockers. 15 min continuous recordings were made before and after cholinergic afferent stimulation.

Oxo-M Local Application

2–3 MΩ patch pipettes filled with Oxo-M were placed in close proximity to identified axons or dendrites 25–30 μm from the somata. 20 ms, 10 psi pressure was applied using a Picospritzer III (Intracel). The puff encompassed an area of approximately 30 μm, indicating that somatic muscarinic receptors were unlikely to be affected.

K_V7 Current Recordings

The external solution was supplemented with 0.001 mM tetrodotoxin (TTx) and 0.1 mM 4-aminopyridine (4-AP). Amphotericin (0.1 mg/ml) was included in the internal solution. Series resistance was between 20 and 40 MΩ and was ~70% compensated. A de-activation protocol (Shah et al., 2008) was applied in the absence and presence of the K_V7 channel blocker, XE991 (3 μM). Recordings were filtered at 1 kHz and sampled at 10 kHz.

T-Type Ca^{2+} Current Measurements

The external solution was supplemented with 0.001 mM TTx, 2 mM $CsCl_2$, 10 mM TEA, 0.1 mM 4-AP, 0.005 mM nifedipine, 0.0001 mM ω-agatoxin IVA, 0.0001 mM ω-conotoxin GVIA, and 0.0002 mM SNX482. The internal pipette solution was 120 mM $CsCl_2$, 1 mM $CaCl_2$, 5 mM $MgCl_2$, 10 mM EGTA, 10 mM HEPES, 2 mM Na_2ATP, 0.3 mM Tris-GTP, and 14 mM Tris-phosphocreatinine (pH 7.3) with KOH, 295–300 mOsm/l. Whole-cell somatic voltage-clamp recordings were made. A 1 s pre-pulse to −100 mV followed by 1 s pulses ranging from −90 mV to −30 mV in 10 mV increments were applied. Leak currents were obtained with 1 s, 10 mV hyperpolarizing steps from −100 mV. All recordings were leak subtracted and TTA-P2 (500 nM) applied at the end. Recordings were filtered at 10 KHz and sampled at 50 kHz.

Electrophysiological Data Analysis

Clampfit (v10.0) was used. The threshold of single action potentials elicited by 30 ms current steps from −70 mV was measured by differentiating the spike voltage with respect to time (dV/dt). This was plotted against the voltage to create a phase plane plot. The threshold was defined as the voltage at the point of deflection for dV/dt to be greater than zero. Action potential height was measured from threshold to the peak, whereas action potential width was the breadth at half the height.

To calculate R_N, we divided the difference in steady-state voltage in the last 25 ms elicited by a 100 pA 400 ms hyperpolarizing step at −70 mV by the applied current. Action potentials elicited by 400 ms depolarizing steps were counted. The peak and area under ADP, if evoked, were also measured.

Cholinergic EPSP summation ratios were calculated as the amplitude of the last EPSP in the train divided by the amplitude of the first EPSP.

The numbers of spontaneous action potentials generated in 15 min during loose cell-attached recordings were counted and the frequency calculated.

For K_V7/M-current voltage-clamp data, the traces obtained in the presence of the XE991 (3 μM) were subtracted from those in the absence. The subtracted traces were fitted with the following to obtain the decay time constants:

$$A_1 e^{(-t/\tau 1)} + A_2 e^{(-t/\tau 2)}$$

where $\tau 1$ and $\tau 2$ represent time constants of the initial and late phase of the K_V7 current.

The K_V7 conductance values were generated from the normalized amplitudes of the subtracted currents (Shah et al., 2008) and were plotted against the voltage. The curves were fitted using the Boltzmann equation:

$$y = A2 + (A1 - A2)/(1 + \exp(-(x - x0/dx)))$$

where A1 and A2 are the initial and maximum values, x0 is the half-activation voltage and dx is the slope of the curve.

Ca^{2+} currents obtained in the presence of TTA-P2 (500 nM) were subtracted from those in the absence of the current to obtain the T-type Ca^{2+} current. The peak current amplitude was plotted against the voltage to obtain the activation curves (Dreyfus et al., 2010). Curves were fitted using the above Boltzmann equation.

Sholl Analysis

A similar method to that described by Huang et al. (2012) was used. Briefly, Confocal (Zeiss LSM 710) images of stained neurons were acquired. In Image J (NIH), 10 μm concentric circles were generated around the somata (Sholl, 1953), the number of dendrites crossing each circle counted.

Two-Photon Ca^{2+} Imaging Experiments

A Prairie Ultima multi-photon microscopy system (Prairie Technologies) was used. The Mai Tai laser (Spectra-Physics) was tuned to 820 nm. Experiments were done at 32°C–34°C. The internal solution was supplemented with a red fluorophore (50 μM Alexa Fluor 594; Invitrogen) and the Ca^{2+}-sensitive green fluorophore, Oregon green BAPTA-1 (200 μM; Invitrogen) for basal $[Ca^{2+}]_i$ measurements. When measuring $[Ca^{2+}]_i$ during action potential waveforms, the Ca^{2+}-sensitive green fluorophore, Fluo-5F (250 μM; Invitrogen) together with Alexa Fluor 594 were utilized (Bender et al., 2010). Cells were filled with dyes for at least 20 min before images were acquired. The granule cell axon

Figure 6. Enhanced T-Type Ca^{2+} Channel Activity Is Required for Muscarinic Receptor-Mediated Persistent Spike Threshold Reduction and K_V7/M Current Suppression

(Ai and Avi) Example traces under control conditions, in the presence of the TTA-P2 (500 nM), either co-application of TTA-P2 and Oxo-M (1 μM) or following HF stimulation in the presence of TTA-P2 and 25 min post-treatment. The RMP values are next to the traces. The insets show 1 s of each trace on an expanded scale. The scales apply to all traces.

(Aii, Aiii, Aiv, Av, and Avii) The action potentials numbers (AP No.) under control conditions, in the presence of a voltage-gated Ca^{2+} channel inhibitors (VGCCI), in the presence of the VCCI either following 10 min Oxo-M treatment or HF stimulation and 25 min post-treatment.

(Bi) Representative single spikes and phase plane plots before and after Oxo-M treatment when TTA-P2 was present.

(Bii) The average spike threshold under control conditions, in the presence of the VCCI and pre- and post-treatment with the VCCI.

(Ci) Example perforated-patch voltage-clamp traces obtained when the de-activation protocol was applied under control conditions, in the presence of TTA-P2, following a 10 min co-application of TTA-P2 and Oxo-M and subsequent application of XE991 (3 μM).

(Cii) The traces obtained in the presence of XE991 were subtracted from all other traces to obtain the K_V7/M currents.

(Ciii) The average K_V7/M current (I_M) amplitude obtained by hyperpolarizing to −50 mV from −20 mV.

(Civ) The apparent activation curve for the K_V7/M currents under control conditions, in the presence of TTA-P2 and during co-application of TTA-P2 and Oxo-M.

A (i) Wildtype Dentate Gyrus Wildtype Dentate Gyrus Wildtype CA3c $Ca_V3.2$ null CA3c (ii)
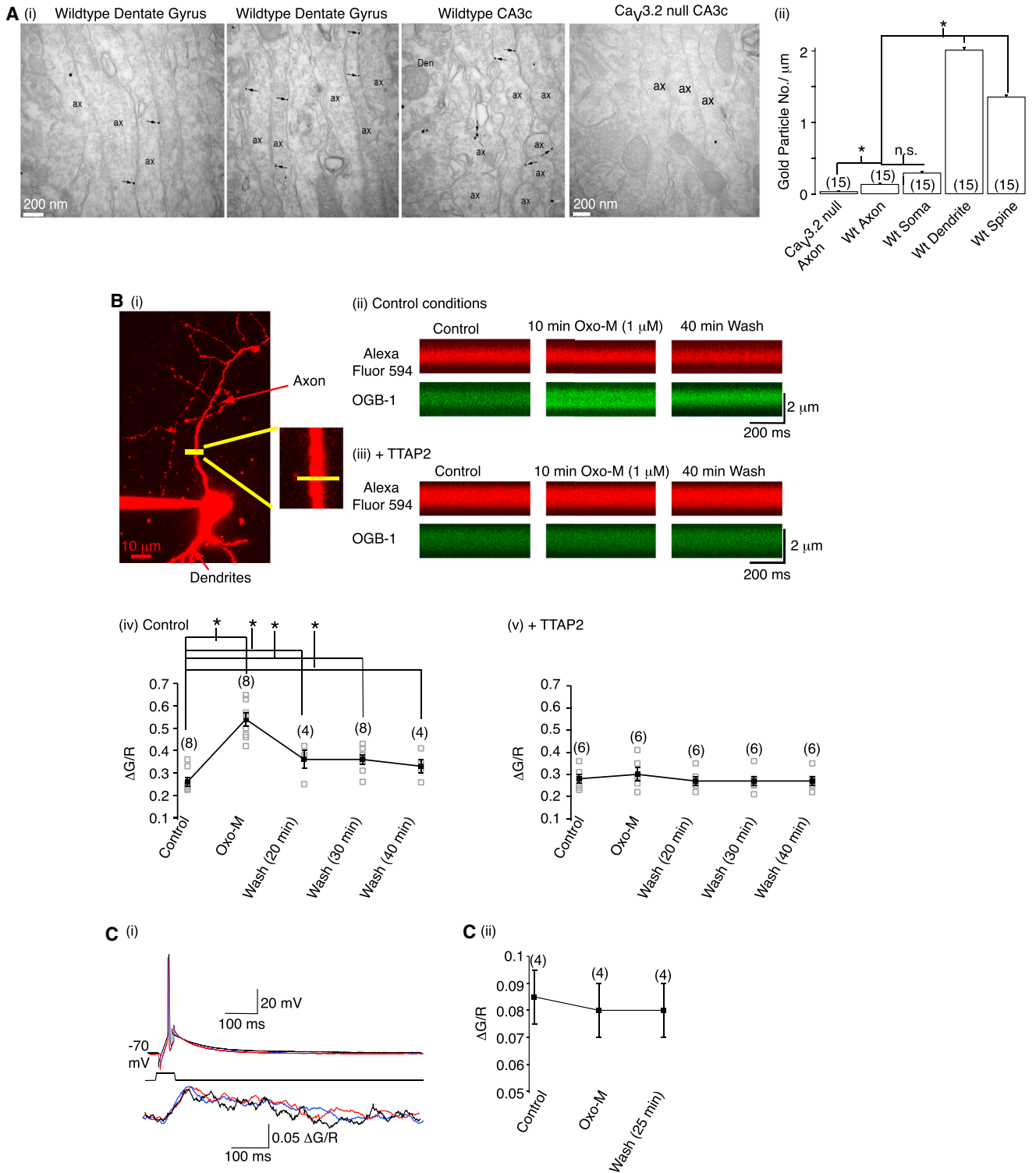
Figure 7. Muscarinic Receptor Activation Induces Sustained Ca^{2+} Entry via Axonal T-Type Ca^{2+} Channels

(Ai) Electron micrographs showing immunogold particles (as indicated by arrows) for $Ca_V3.2$ subunits. Scale bar, 0.2 μm.

(Aii) Immunogold particle quantification in dentate gyrus.

(Bi) A two-photon image of a granule cell filled with Alexa Fluor 594 for 30 min. Cross-section line scans were obtained approximately 25 μm from the cell body as shown by the yellow bar.

(legend continued on next page)
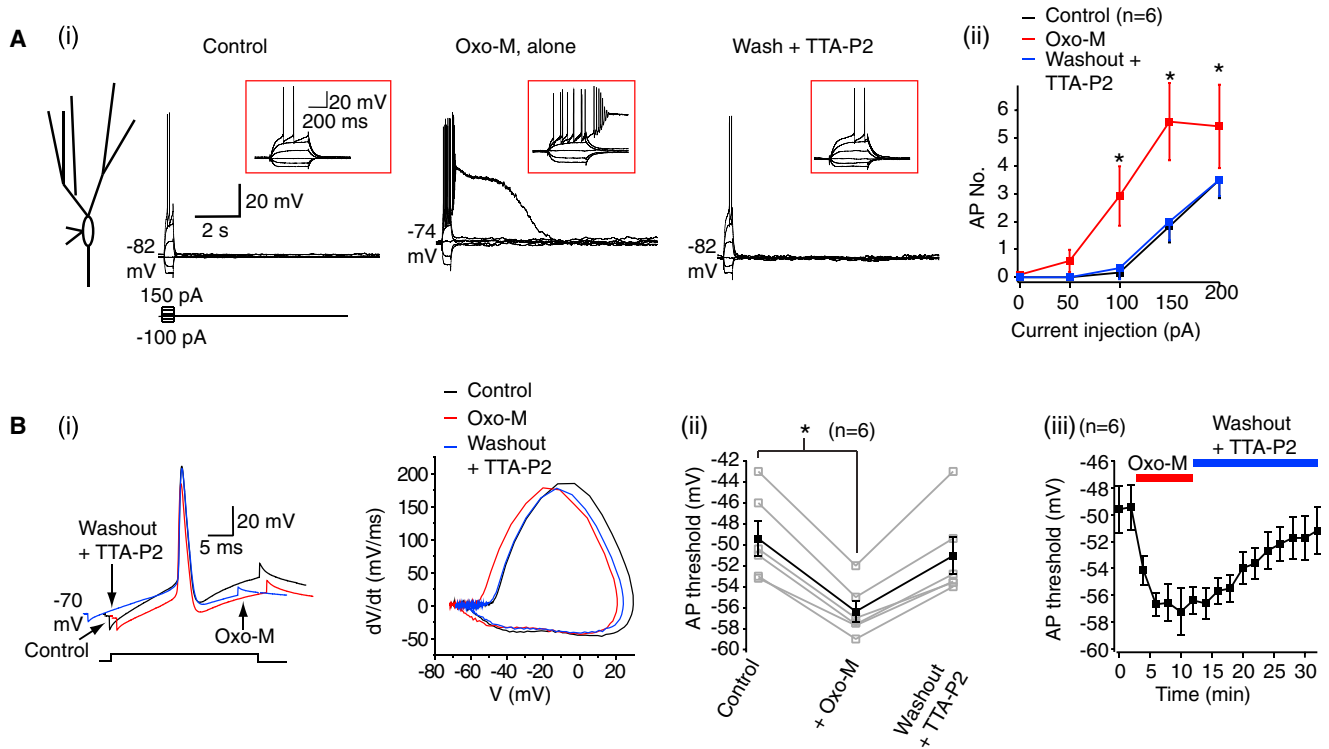
Figure 8. T-Type Ca²⁺ Channel Antagonists Restore Muscarinic Receptor-Induced Spike Threshold Alterations

(Ai) Typical traces under control conditions, following Oxo-M treatment, and after Oxo-M washout during which TTA-P2 (500 nM) was included. The RMP values are adjacent to the traces. The insets show the traces on an expanded timescale. The scale bars apply to all traces.

(Aii) The average action potential number (AP. No.) under control conditions, in the presence of Oxo-M and with TTA-P2 included in the external solution during the washout of Oxo-M.

(Bi) Example single action potentials and phase plane plots before, during, and after Oxo-M treatment. TTA-P2 was included in the external solution during the washout.

(Bii) Individual (open gray squares) and mean (black filled squares) spike threshold values before, during, and after Oxo-M treatment when TTA-P2 was included in the solution.

(Biii) Time course to show the recovery of the action potential threshold following Oxo-M treatment when TTA-P2 is included in the external solution during washout.

was identified as the process that lacked spines. At least three cross-sectional line scans were made at 667 Hz in the distal axon initial segment (25–30 μm from soma; Figure 7B) and averaged to obtain the signal. Background currents were recorded at the end of experiments. The fluorescence was quantified as:

$$\Delta G/R = \left(F_{green} - F_{dark\ green}\right)/\left(F_{red} - I_{dark,\ red}\right).$$

F_{green} and F_{red} are the green and red fluorescence signals and $F_{dark\ green}$ and $I_{dark,\ red}$ are the background currents in the green and red channels, respectively.

Electron Microscopy Experiments

Three adult rats and Ca$_V$3.2 null mice were deeply anesthetized by intraperitoneal injection of ketamine-xylazine 1:1 (0.1 ml/kg) and transcardially perfused with ice-cold fixative containing 4% paraformaldehyde, 0.05%

glutaraldehyde, and 15% saturated picric acid in 0.1 M phosphate buffer (PB, pH 7.4). After perfusion, brains were removed and immersed in the fixative for 2 hr or overnight at 4°C. Tissue blocks were washed in 0.1 M PB. 60 μm coronal sections were cut with a Vibratome (Leica V1000). Free-floating sections were incubated in 10% NGS diluted in TBS, then with the primary antibodies (2–5 μg/ml), followed by goat anti-rabbit or goat anti-mouse IgG coupled to 1.4 nm gold (Nanoprobes). Sections were post-fixed in 1% glutaraldehyde and washed in double-distilled water, followed by silver enhancement of the gold particles with an HQ Silver kit (Nanoprobes). Sections were then treated with osmium tetraoxide (1% in 0.1 M PB), block stained with uranyl acetate, dehydrated in graded series of ethanol, and flat embedded on glass slides in Durcupan (Fluka) resin. Regions of interest (ROIs) were cut at 70–90 nm on an ultramicrotome (Reichert Ultracut E, Leica) and collected on 200-mesh copper grids. Staining was performed on drops of 1% aqueous uranyl acetate followed by Reynolds's lead citrate.

(Bii and Biii) Average line scan images obtained using Alexa Fluor 594 and Oregon green Bapta-1 (OGB-1) under control conditions, after 10 min Oxo-M (1 μM), and following 40 min washout of Oxo-M in the absence and presence of TTA-P2 (500 nM), respectively.

(Biv and Bv) Individual (gray open squares) and average (black filled squares) ΔG/R measurements before, after Oxo-M treatment, and following Oxo-M washout in the absence and presence of TTA-P2.

(Ci) Superimposed example single action potentials and associated axonal [Ca²⁺]ᵢ signals before, during, and after 25 min washout of Oxo-M.

(Cii) Average ΔG/R measurements for action potential-associated [Ca²⁺]ᵢ signals under control conditions, after 10 min Oxo-M application, and following 25 min washout of Oxo-M.

Ultrastructural analyses were performed with a Jeol-1010 electron microscope (Japan).

Affinity-purified rabbit anti-M1 was characterized previously (Yamasaki et al., 2010). The monoclonal antibody against Ca$_V$3.2 (Clone N55/10) was obtained from the NeuroMab Facility (University of California, Davis). No labeling was observed if the primary antibody was either omitted or replaced with 5% (v/v) normal serum.

Light Microscopy Experiments

All procedures were approved by the Animal Care and Use Committee of Baylor College of Medicine.

Colocalization of AISs and Cholinergic Fibers

Three postnatal days 22–29 Sprague-Dawley rats were deeply anesthetized and perfused with PBS containing 4% paraformaldehyde and 0.1% glutaraldehyde. Brains were removed, kept at 4°C overnight in the fixative, and then stored in PBS. 40 μm floating sections were cut (VT1200S, Leica), rinsed in PBS, blocked, and permeabilized for 1 hr at room temperature and incubated with primary antibodies overnight (mouse α-ChAT, Chemicon; rabbit α-βIV-Spectrin [Ogawa et al., 2006]). Sections were washed extensively, incubated with secondary antibodies (goat α-mouse IgG1 γ1 555, Invitrogen; donkey α-rabbit DyLight 488, Jackson), washed again, and coverslipped (Prolong Gold with DAPI, Invitrogen). Image stacks were acquired using a C2 laser-scanning confocal microscope (Nikon). Maximal intensity projections of z stacks 3D views, and movies were created using NIS-Elements.

Quantification of KCNQ2 and KCNQ2 Immunolabeling

Hippocampal slices were treated with either vehicle (control) or Oxo-M (1 μM), irradiated in sodium citrate-EDTA buffer (pH 8.5) using a microwave oven (Sears), then washed in PBS, blocked for 1 hr at room temperature, and incubated with primary antibodies for 48 hr (mouse α-PanNaV IgG1, Sigma; rabbit α-KCNQ2n; guinea pig α-KCNQ3n) followed by incubation with secondary antibodies (donkey α-mouse-Cy3, Jackson; donkey α-rabbit-DyLight 488, Jackson; donkey α-guinea pig-Cy5, Jackson). Image stacks were acquired using a Nikon C2 laser-scanning confocal microscope. Four regions of interest (ROIs) spanning the dentate granule cell layer were analyzed. ROI dimensions were 92.3 μm × 46.1 μm × 20.3 μm deep. Five AISs in each ROI were analyzed for length and labeling intensity. Using maximal projection and 3D views in NIS-Elements, we drew a 3D polyline along the axon, from soma to beyond the AIS. This was converted to a 2D (xy versus z) plot and labeling at each pixel along the trajectory for each fluorophore was read. Pixel intensities normalized to the max intensity for each fluorophore. For each group, AIS lengths were estimated from Na$_V$ staining and normalized to an average AIS length. Raw pixel intensities, without background subtraction, were binned in 2 μm lengths and averaged per bin for each group.

Statistical Methods

Group data are expressed as mean ± SEM. Statistical significance was determined using either paired or unpaired Student's t tests as appropriate. Statistical significance of differences at $p < 0.05$ is indicated as asterisks (*) in all figures.

SUPPLEMENTAL INFORMATION

Supplemental Information includes eight figures, four tables, and one movie and can be found with this article online at http://dx.doi.org/10.1016/j.neuron.2014.12.030.

AUTHOR CONTRIBUTIONS

K.M., Z.H., R.L., B.T., E.C., and M.M.S. performed experiments and analyzed data. M.W. contributed valuable re-agents. M.M.S., R.L., E.C., and D.A.B. designed experiments. M.M.S. and D.A.B. wrote the manuscript, with contributions from all authors.

REFERENCES

Acsády, L., and Káli, S. (2007). Models, structure, function: the transformation of cortical signals in the dentate gyrus. Prog. Brain Res. 163, 577–599.

Alkondon, M., Pereira, E.F., Wonnacott, S., and Albuquerque, E.X. (1992). Blockade of nicotinic currents in hippocampal neurons defines methyllycaconitine as a potent and specific receptor antagonist. Mol. Pharmacol. 41, 802–808.

Aznavour, N., Watkins, K.C., and Descarries, L. (2005). Postnatal development of the cholinergic innervation in the dorsal hippocampus of rat: Quantitative light and electron microscopic immunocytochemical study. J. Comp. Neurol. 486, 61–75.

Battefeld, A., Tran, B.T., Gavrilis, J., Cooper, E.C., and Kole, M.H. (2014). Heteromeric Kv7.2/7.3 channels differentially regulate action potential initiation and conduction in neocortical myelinated axons. J. Neurosci. 34, 3719–3732.

Bean, B.P. (2007). The action potential in mammalian central neurons. Nat. Rev. Neurosci. 8, 451–465.

Bender, K.J., Ford, C.P., and Trussell, L.O. (2010). Dopaminergic modulation of axon initial segment calcium channels regulates action potential initiation. Neuron 68, 500–511.

Brazhnik, E.S., and Fox, S.E. (1999). Action potentials and relations to the theta rhythm of medial septal neurons in vivo. Exp. Brain Res. 127, 244–258.

Brown, D.A., and Passmore, G.M. (2009). Neural KCNQ (Kv7) channels. Br. J. Pharmacol. 156, 1185–1195.

Buchanan, K.A., Petrovic, M.M., Chamberlain, S.E., Marrion, N.V., and Mellor, J.R. (2010). Facilitation of long-term potentiation by muscarinic M(1) receptors is mediated by inhibition of SK channels. Neuron 68, 948–963.

Buzsáki, G. (2002). Theta oscillations in the hippocampus. Neuron 33, 325–340.

Catterall, W.A. (2011). Voltage-gated calcium channels. Cold Spring Harb. Perspect. Biol. 3, a003947.

Cole, A.E., and Nicoll, R.A. (1983). Acetylcholine mediates a slow synaptic potential in hippocampal pyramidal cells. Science 221, 1299–1301.

Cooper, E.C., Harrington, E., Jan, Y.N., and Jan, L.Y. (2001). M channel KCNQ2 subunits are localized to key sites for control of neuronal network oscillations and synchronization in mouse brain. J. Neurosci. 21, 9529–9540.

Coulter, D.A., and Carlson, G.C. (2007). Functional regulation of the dentate gyrus by GABA-mediated inhibition. Prog. Brain Res. 163, 235–243.

Debanne, D., Campanac, E., Bialowas, A., Carlier, E., and Alcaraz, G. (2011). Axon physiology. Physiol. Rev. 91, 555–602.

Devaux, J.J., Kleopa, K.A., Cooper, E.C., and Scherer, S.S. (2004). KCNQ2 is a nodal K+ channel. J. Neurosci. 24, 1236–1244.

Dreyfus, F.M., Tscherter, A., Errington, A.C., Renger, J.J., Shin, H.S., Uebele, V.N., Crunelli, V., Lambert, R.C., and Leresche, N. (2010). Selective T-type calcium channel block in thalamic neurons reveals channel redundancy and physiological impact of I(T)window. J. Neurosci. 30, 99–109.

Falkenburger, B.H., Dickson, E.J., and Hille, B. (2013). Quantitative properties and receptor reserve of the DAG and PKC branch of G(q)-coupled receptor signaling. J. Gen. Physiol. 141, 537–555.

Gamper, N., and Shapiro, M.S. (2007). Regulation of ion transport proteins by membrane phosphoinositides. Nat. Rev. Neurosci. 8, 921–934.

Grubb, M.S., and Burrone, J. (2010). Building and maintaining the axon initial segment. Curr. Opin. Neurobiol. 20, 481–488.

Gu, Z., and Yakel, J.L. (2011). Timing-dependent septal cholinergic induction of dynamic hippocampal synaptic plasticity. Neuron 71, 155–165.

Hasselmo, M.E., and Sarter, M. (2011). Modes and models of forebrain cholinergic neuromodulation of cognition. Neuropsychopharmacology 36, 52–73.

Henze, D.A., Wittner, L., and Buzsáki, G. (2002). Single granule cells reliably discharge targets in the hippocampal CA3 network in vivo. Nat. Neurosci. 5, 790–795.

Huang, Z., Lujan, R., Martinez-Hernandez, J., Lewis, A.S., Chetkovich, D.M., and Shah, M.M. (2012). TRIP8b-independent trafficking and plasticity of adult cortical presynaptic HCN1 channels. J. Neurosci. 32, 14835–14848.

Jones, B.E. (2004). Activity, modulation and role of basal forebrain cholinergic neurons innervating the cerebral cortex. Prog. Brain Res. 145, 157–169.

Kole, M.H., and Stuart, G.J. (2012). Signal processing in the axon initial segment. Neuron 73, 235–247.

Krueppel, R., Remy, S., and Beck, H. (2011). Dendritic integration in hippocampal dentate granule cells. Neuron 71, 512–528.

Lee, M.G., Hassani, O.K., Alonso, A., and Jones, B.E. (2005). Cholinergic basal forebrain neurons burst with theta during waking and paradoxical sleep. J. Neurosci. 25, 4365–4369.

Leterrier, C., and Dargent, B. (2014). No Pasaran! Role of the axon initial segment in the regulation of protein transport and the maintenance of axonal identity. Semin. Cell Dev. Biol. 27, 44–51.

Lübke, J., Frotscher, M., and Spruston, N. (1998). Specialized electrophysiological properties of anatomically identified neurons in the hilar region of the rat fascia dentata. J. Neurophysiol. 79, 1518–1534.

Lukacs, V., Yudin, Y., Hammond, G.R., Sharma, E., Fukami, K., and Rohacs, T. (2013). Distinctive changes in plasma membrane phosphoinositides underlie differential regulation of TRPV1 in nociceptive neurons. J. Neurosci. 33, 11451–11463.

Ogawa, Y., Schafer, D.P., Horresh, I., Bar, V., Hales, K., Yang, Y., Susuki, K., Peles, E., Stankewich, M.C., and Rasband, M.N. (2006). Spectrins and ankyrinB constitute a specialized paranodal cytoskeleton. J. Neurosci. 26, 5230–5239.

Ohkuma, M., Kawai, F., and Miyachi, E. (2013). Acetylcholine enhances excitability by lowering the threshold of spike generation in olfactory receptor cells. J. Neurophysiol. 110, 2082–2089.

Papke, R.L., Wecker, L., and Stitzel, J.A. (2010). Activation and inhibition of mouse muscle and neuronal nicotinic acetylcholine receptors expressed in Xenopus oocytes. J. Pharmacol. Exp. Ther. 333, 501–518.

Park, J.Y., and Spruston, N. (2012). Synergistic actions of metabotropic acetylcholine and glutamate receptors on the excitability of hippocampal CA1 pyramidal neurons. J. Neurosci. 32, 6081–6091.

Park, J.Y., Kang, H.W., Moon, H.J., Huh, S.U., Jeong, S.W., Soldatov, N.M., and Lee, J.H. (2006). Activation of protein kinase C augments T-type Ca2+ channel activity without changing channel surface density. J. Physiol. 577, 513–523.

Pelkey, K.A., and McBain, C.J. (2008). Target-cell-dependent plasticity within the mossy fibre-CA3 circuit reveals compartmentalized regulation of presynaptic function at divergent release sites. J. Physiol. 586, 1495–1502.

Pernía-Andrade, A.J., and Jonas, P. (2014). Theta-gamma-modulated synaptic currents in hippocampal granule cells in vivo define a mechanism for network oscillations. Neuron 81, 140–152.

Picciotto, M.R., Higley, M.J., and Mineur, Y.S. (2012). Acetylcholine as a neuromodulator: cholinergic signaling shapes nervous system function and behavior. Neuron 76, 116–129.

Schmidt-Hieber, C., and Bischofberger, J. (2010). Fast sodium channel gating supports localized and efficient axonal action potential initiation. J. Neurosci. 30, 10233–10242.

Selyanko, A.A., and Brown, D.A. (1996). Intracellular calcium directly inhibits potassium M channels in excised membrane patches from rat sympathetic neurons. Neuron 16, 151–162.

Shah, M.M., Migliore, M., Valencia, I., Cooper, E.C., and Brown, D.A. (2008). Functional significance of axonal Kv7 channels in hippocampal pyramidal neurons. Proc. Natl. Acad. Sci. USA 105, 7869–7874.

Shen, W., Hamilton, S.E., Nathanson, N.M., and Surmeier, D.J. (2005). Cholinergic suppression of KCNQ channel currents enhances excitability of striatal medium spiny neurons. J. Neurosci. 25, 7449–7458.

Sholl, D.A. (1953). Dendritic organization in the neurons of the visual and motor cortices of the cat. J. Anat. 87, 387–406.

Simon, A.P., Poindessous-Jazat, F., Dutar, P., Epelbaum, J., and Bassant, M.H. (2006). Firing properties of anatomically identified neurons in the medial septum of anesthetized and unanesthetized restrained rats. J. Neurosci. 26, 9038–9046.

Skaggs, W.E., McNaughton, B.L., Wilson, M.A., and Barnes, C.A. (1996). Theta phase precession in hippocampal neuronal populations and the compression of temporal sequences. Hippocampus 6, 149–172.

Yamasaki, M., Matsui, M., and Watanabe, M. (2010). Preferential localization of muscarinic M1 receptor on dendritic shaft and spine of cortical pyramidal cells and its anatomical evidence for volume transmission. J. Neurosci. 30, 4408–4418.

Cholinergic Afferent Stimulation

Induces Axonal Function Plasticity

# in Adult Hippocampal Granule Cells

Katiuscia Martinello, Zhuo Huang, Rafael Lujan, Baouyen Tran, Masahiko Watanabe, Edward C. Cooper, David A. Brown, and Mala M. Shah
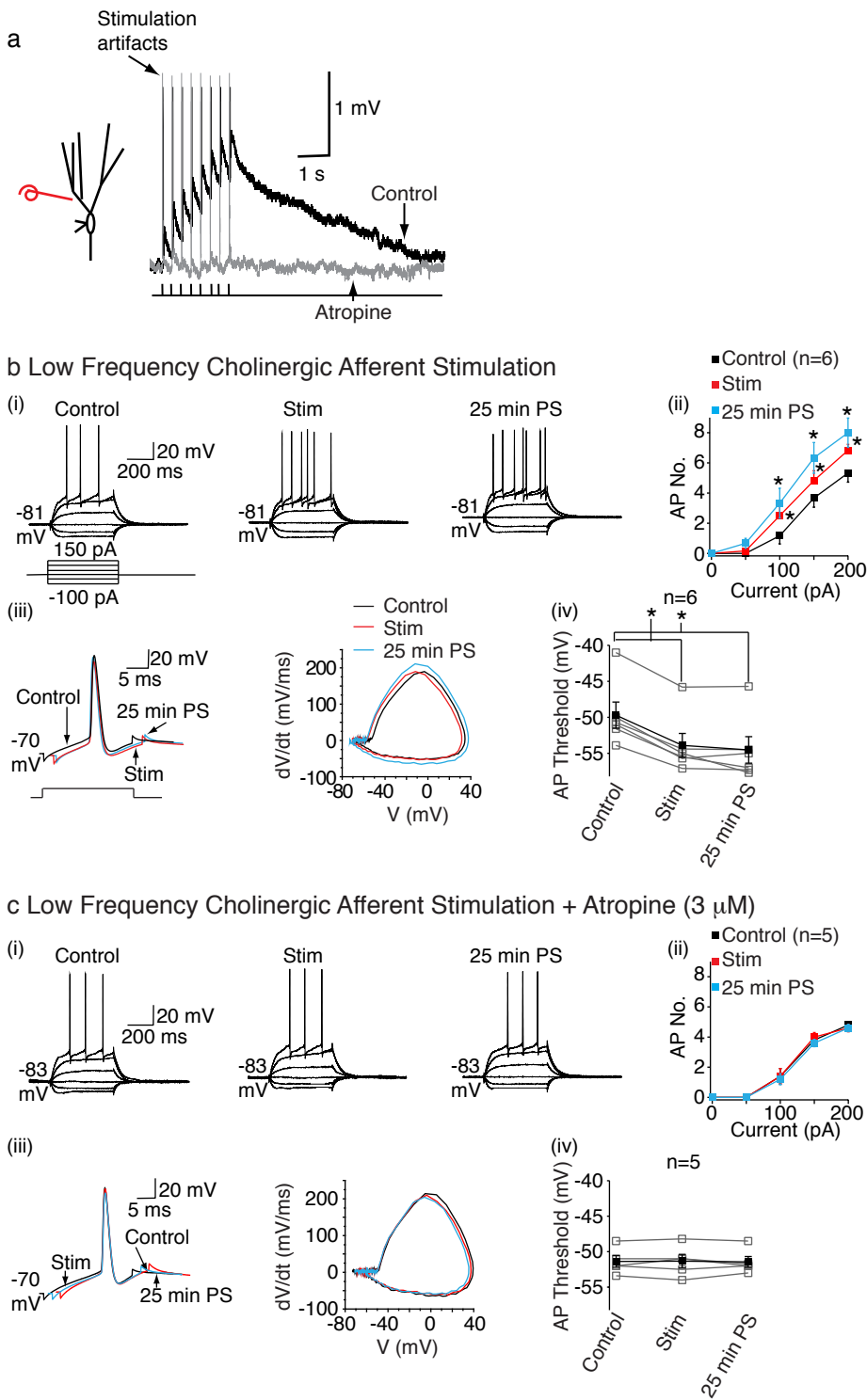
Supp Fig 1 (linked to Fig 1): Intrinsic plasticity induced by low frequency cholinergic afferent stimulation. a Example cholinergic synaptic potentials in the absence (control) and presence of atropine (3 μM). Eight cholinergic synaptic potentials (0.8 Hz; shown in inset) were generated every 325 ms as depicted in the schematic. The stimulation pattern was repeated ten times at 0.1 Hz. **b(i)** and **c(i)** Representative traces obtained in response to a series of 400 ms hyperpolarizing and depolarizing current pulses before, immediately after stimulation (stim) and 25 min post stimulation (PS) in long axon granule cells with and without atropine respectively. The RMP values are indicated adjacent to the traces. The scale shown applies to all traces. **b(ii)** and **c(ii)** Graph depicting the average action potential numbers (AP No.) elicited by depolarizing current steps. **b(iii)** and **c(iii)** Example single action potentials obtained at -70 mV prior, immediately after and 25 min post stimulation in the absence and presence of atropine respectively. The phase plane plots are shown on the right. **b(iv)** and **c(iv)** Individual (open square) and mean (filled squares) action potential threshold values before and after stimulation under control conditions and in the presence of atropine respectively.
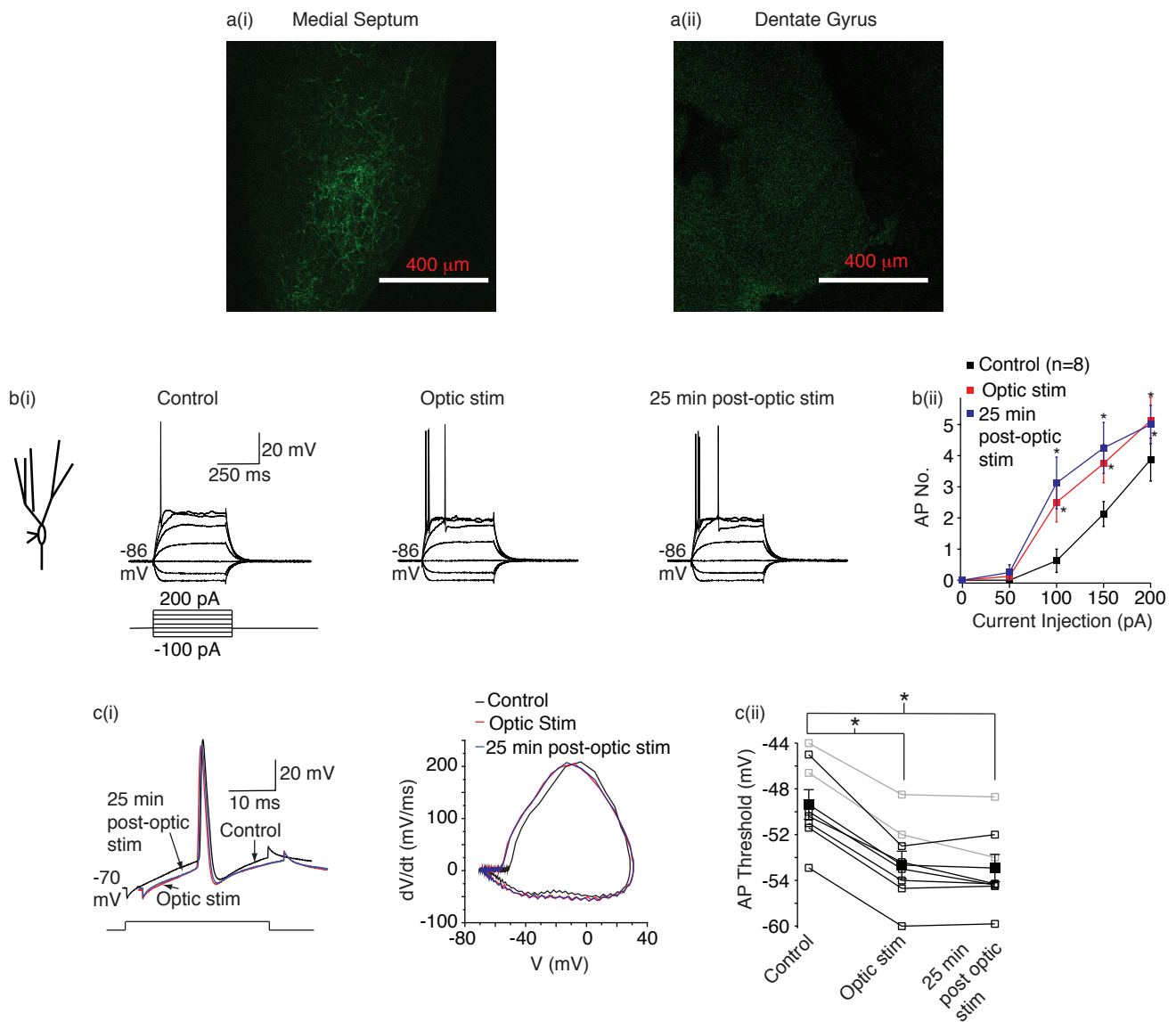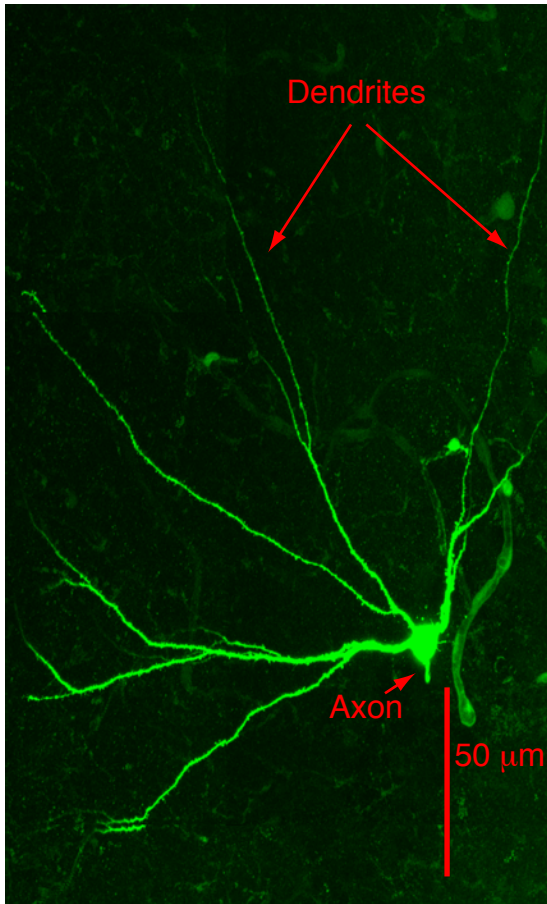
Supp Fig 2: Persistent reduction in spike threshold induced by optical stimulation of cholinergic fibers a(i) Confocal images showing eYFP labelled cholinergic fibers in the medial septum **a(ii)** Confocal images showing eYFP labelled puncta in the dentate gyrus. Both images were taken with same settings and magnification. **b(i)** Example traces recorded from granule cell soma in response to 400 ms long square pulses as indicated in the schematic below before, immediately after and 25 min following optical stimulation (optic stim) of cholinergic fibers in the dentate gyrus region. The RMP values are recorded adjacent to each trace. The scale on the first trace applies to all traces within **b(i)**. **b(ii)** The average numbers of action potentials (AP No.) in response to 400 ms current injections of varying amplitudes. Note that in 6/8 experiments the glutamate and GABA receptor blockers were present. Since there was little difference between experiments in which the blockers were present and those in which they were absent the data were pooled together. **c(i)** Representative single action potentials elicited by a short pulse at -70 mV prior to, immediately after and 25 min post optical stimulation of cholinergic fibers. The associated phase plane plots are shown on the right. **c(ii)** Individual (open squares) and mean (filled square) action potential (AP) threshold values under control conditions and either immediately after or 25 min after optical stimulation of cholinergic fibers. Grey squares represent experiments in which glutamate and GABA receptor blockers were omitted. The data from all experiments irrespective of whether glutamate and GABA receptor blockers were present were pooled together to obtain the mean and SEM values. Asterisks indicate significance at $p < 0.05$.
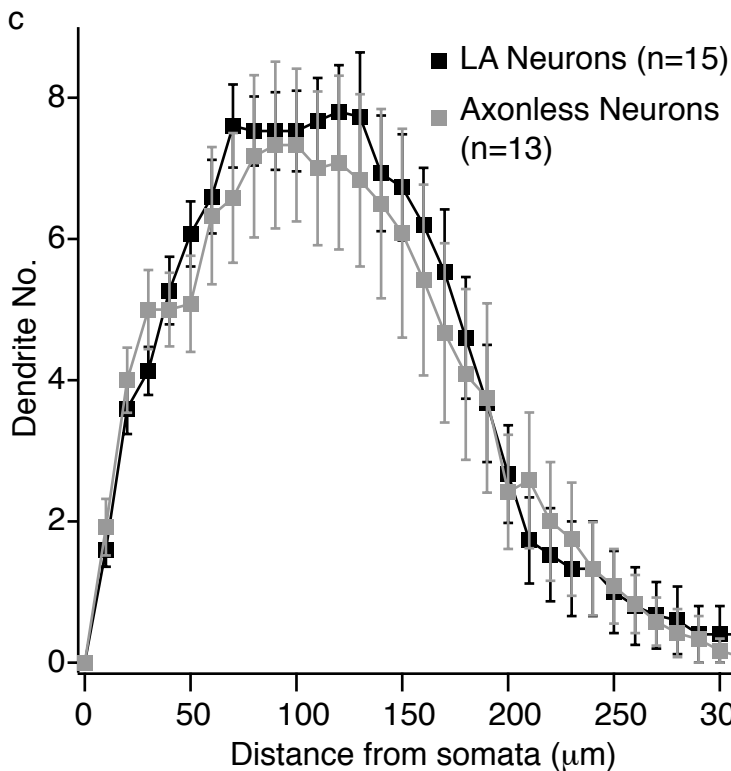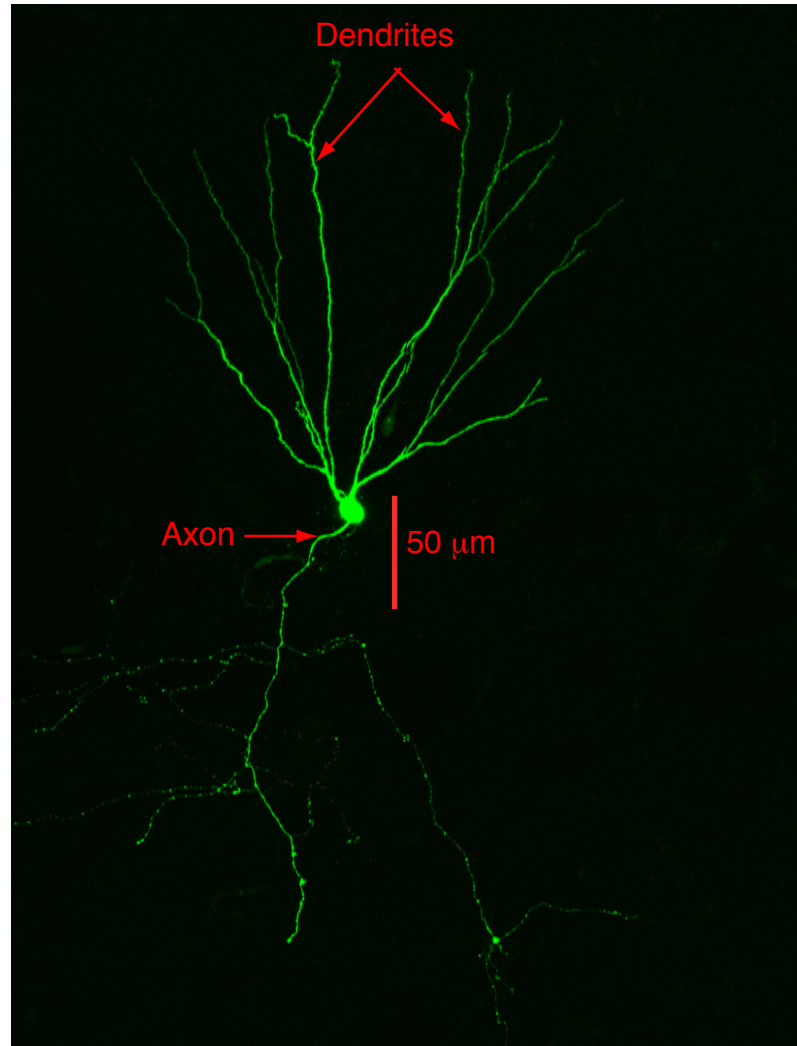
Martinello et al. Supp Fig 3
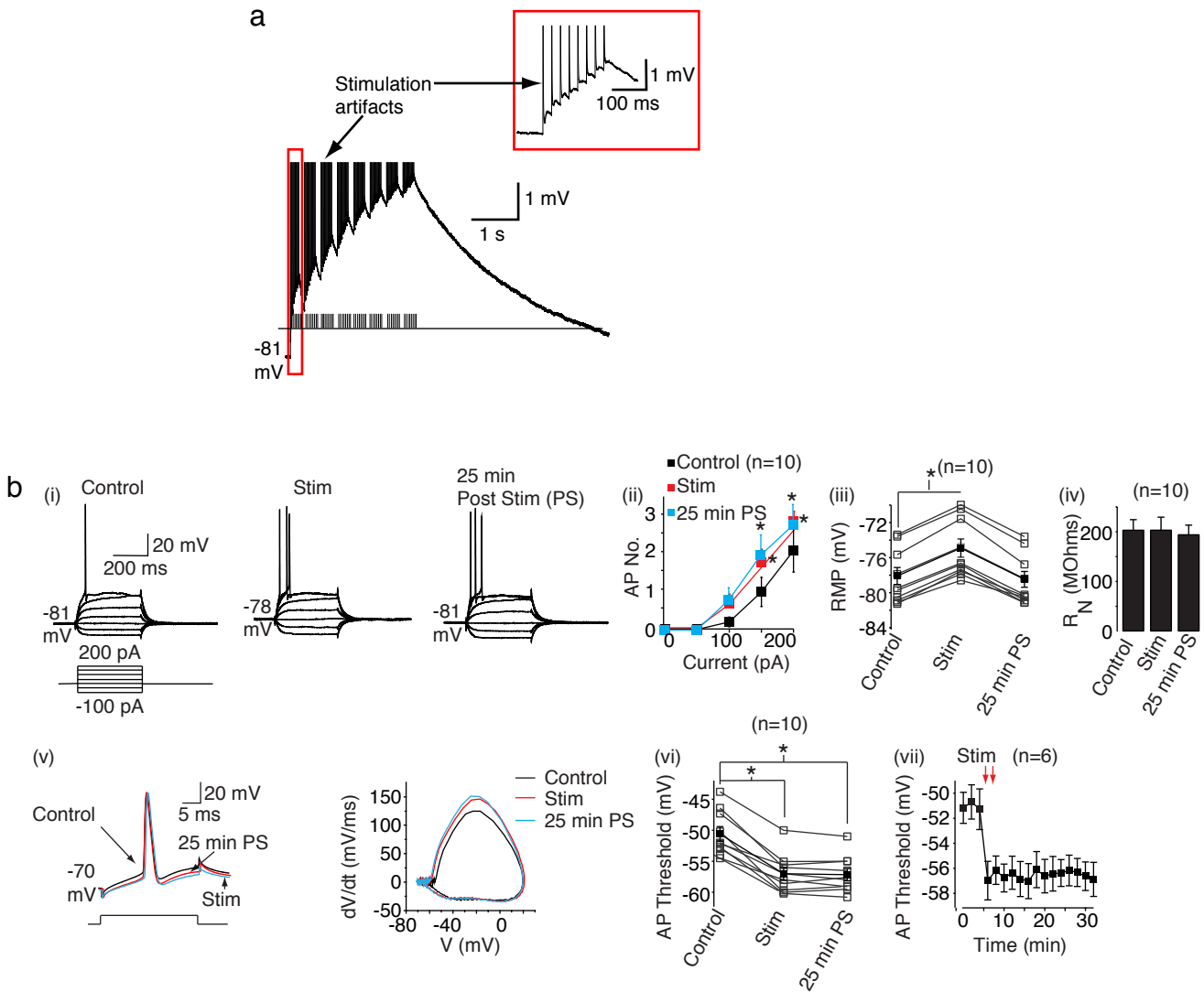
Supp Fig 3 (linked to Fig 1): Neostigmine boosts cholinergic EPSPs and associated action potential threshold plasticity. a Example cholinergic EPSPs obtained by stimulation of cholinergic fibers in the presence of the anticholinersterase inhibitor, neostigmine (3 μM). The inset shows the first burst of EPSPs on an enhanced time scale. **b(i)** Representative traces obtained in response to a series of 400 ms hyperpolarizing and depolarizing current pulses before, immediately after stimulation (stim) and 25 min post stimulation (PS) in long axon granule cells. The RMP values are indicated adjacent to the traces. The scale shown applies to all traces. **(ii)** Graph depicting the average action potential numbers (AP No.) elicited by depolarizing current steps. **(iii)** The individual (open squares) and mean (filled squares) RMP values before, following and 25 min post stimulation. **(iv)** Average input resistance (R_N) values. **(v)** Example single action potentials obtained at -70 mV prior, immediately after and 25 min post stimulation. The associated phase plane plots are shown on the right. **(vi)** Individual (open square) and mean (filled squares) action potential threshold values before and after stimulation. **(vii)** Graph showing the timecourse of the change in action potential threshold values post stimulation.

a Axonless Cell

Dendrites

Axon

50 μm

b Long Axon (LA) Neuron

Dendrites

Axon

50 μm

c

■ LA Neurons (n=15)
■ Axonless Neurons (n=13)

Dendrite No.

Distance from somata (μm)

Supp Fig 4 (linked to Fig 2): Sholl analysis of axonless and long axon neuron dendritic trees. a and b Typical images of axonless and long axon neurons respectively obtained using a Zeiss 710 confocal microscope. The neurons had been filled with neurobiotin (2 % w/v), fixed with 4 % paraformaldehyde and stained using streptavidin alexa fluor 488 antibodies. Axonless neurons had an average residual axon length of 6.1 ± 1.2 μm whilst long axon neurons had axons greater than 100 μm long. The images were imported into Image J (NIH) and 10 μm apart concentric circles were constructed around the somata in Image J. The number of dendrites crossing each concentric circle were counted. **c** Plot of the mean and SEM number of dendrites against distance from the somata (Sholl analysis).
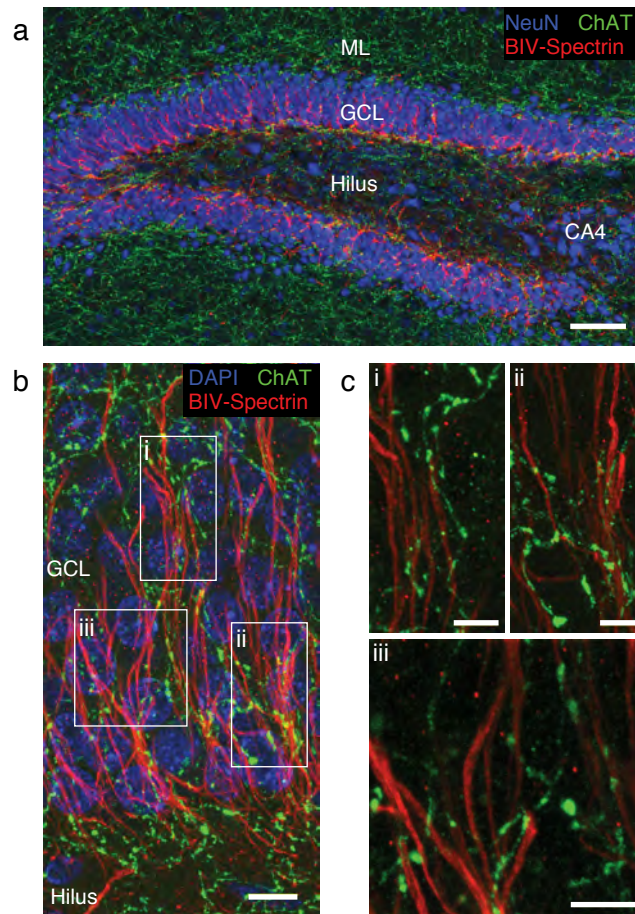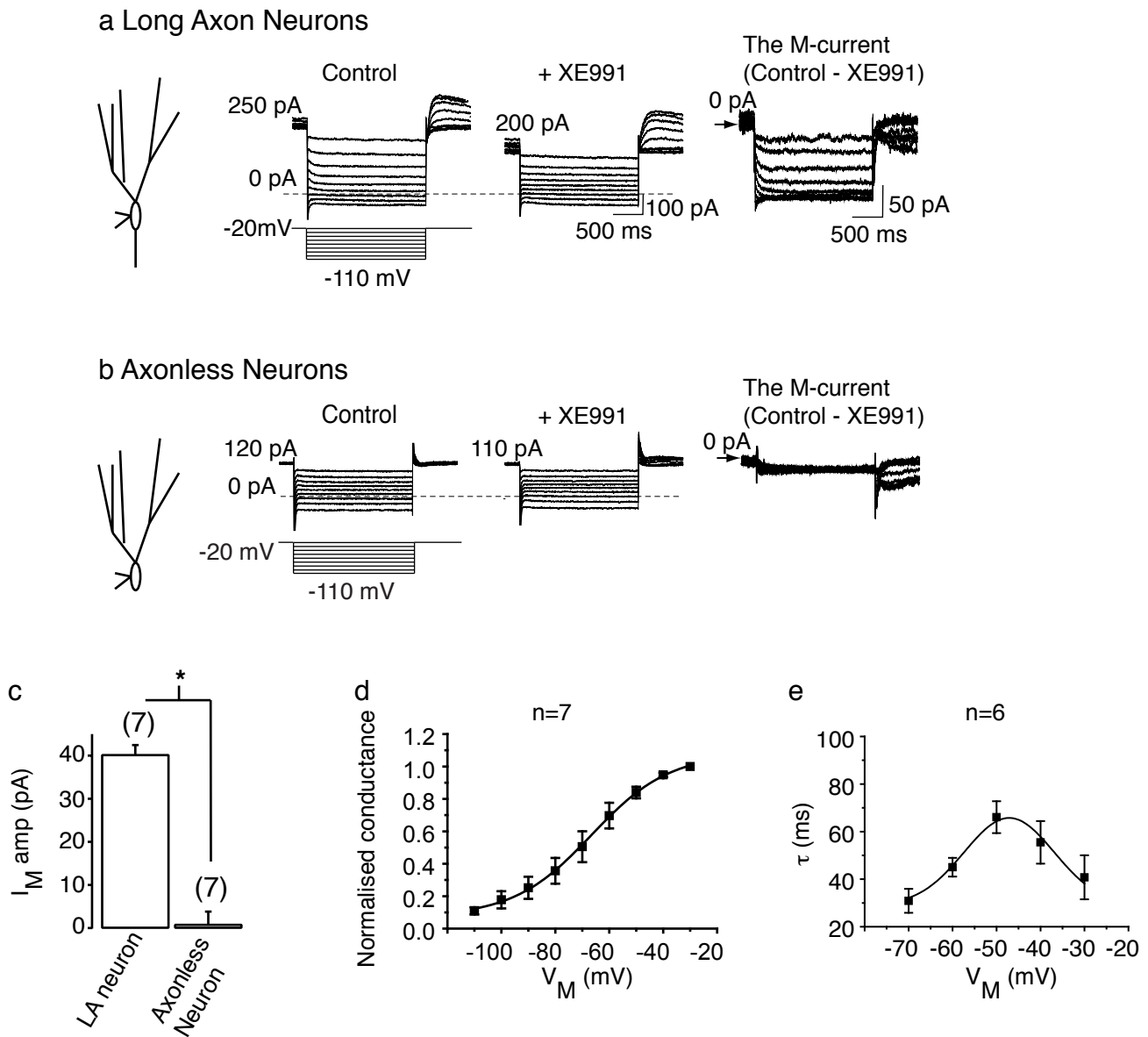
Supp Fig 5: Cholinergic fibers are abundant in the dentate gyrus and lie near granule cell axon initial segments (AISs). a Low magnification image showing cholinergic fibers (ChAT, green) are numerous in the molecular layer (ML) and hilus, and more sparse within the granule cell layer (GCL). Cell bodies are labelled with antibodies against the neuron specific protein, NeuN. **b** 15 μm deep maximum intensity projection view of the GCL demonstrating that AISs labelled with βIV spectrin are clustered within columns that are perpendicular to the hilar border. Cell nuclei are labelled with DAPI. Cholinergic fibers detected with ChAT antibodies are enriched within these columns, and sometimes follow the paths of AISs. Boxes enclose regions shown at higher magnification in **c. c** Close proximity of dentate granule cell AISs and ChAT fibers in thin maximal intensity projections ((i)10 μm deep, (ii)15 μm and (iii) 10 μm). Scale bars: a 50 μm; b, 10 μm; c, 5 μm
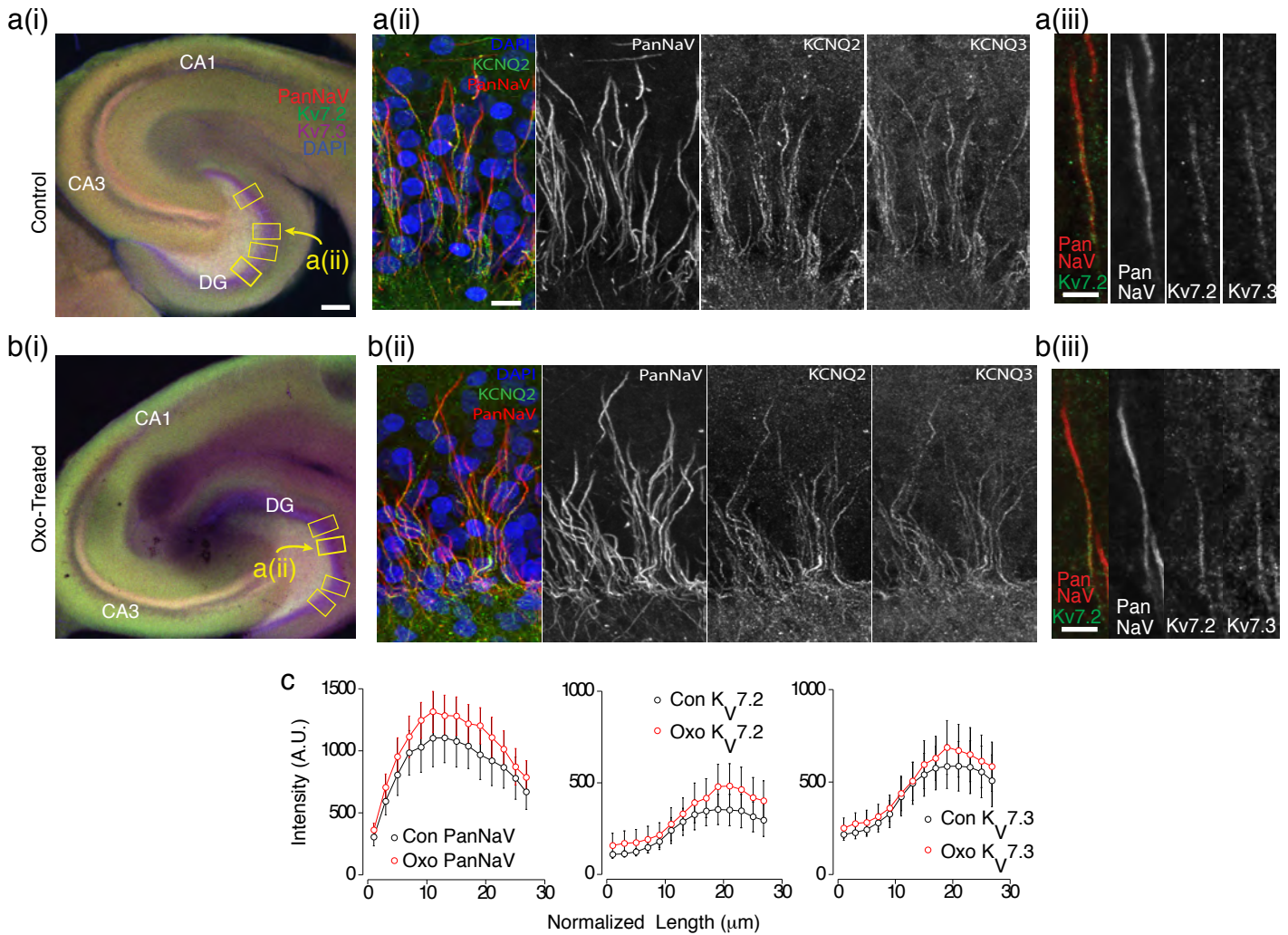
Supp. Fig 6: Na$_V$ and K$_V$7 channel localisation not altered by acute muscarinic receptor stimulation. Example images of p22 -27 rat slices treated for 10 min with either vehicle (control, **a**) or oxotremorine-M (Oxo-M, **b**) labelled with antibodies against NaV (PanNaV), K$_V$7.2 and K$_V$7.3 subunits. The slices were also treated with DAPI to label nuclei of neurons. a(i), b(i) Low magnification images that show labelling for PanNaV, K$_V$7.2 and K$_V$7.3 is most conspicuous along the mossy fiber pathway within the hilus and stratum lucidum of CA3. Boxes show regions of interest (ROIs) where axon initial segment (AIS) labelling intensity was quantified. The ROIs are shown at higher magnification in **a(ii)** and **b(ii)** respectively. **a(iii), b(iii)** Examples of individual AISs in vehicle and Oxo-M treated slices. There is no discernable differences in labelling of K$_V$7.2/7.3 within the AIS between these. **c** Plots of normalised relative intensity of K$_V$7.2/7.3 and PanNaV between control (con; n=3 slices) and Oxo-M (n=3 slices)-treated groups. There is no signficant difference in intensity values within the granule cell AISs between control- and Oxo-M treated groups. Scale bars: **a(i), b(i)**, 100 μm; **a(ii), b(ii)**, 10 μm; **a(iii), b(iii)**, 5 μm. A.U.: arbitrary units.

a Long Axon Neurons

Control　　+ XE991　　The M-current (Control - XE991)

250 pA　200 pA　0 pA

0 pA

-20mV

-110 mV

100 pA　500 ms　50 pA　500 ms

b Axonless Neurons

Control　　+ XE991　　The M-current (Control - XE991)

120 pA　110 pA　0 pA

0 pA

-20 mV

-110 mV

c (7) (7) *

I_M amp (pA)

LA neuron　Axonless Neuron

d n=7

Normalised conductance

V_M (mV)

e n=6

τ (ms)

V_M (mV)

Supp Fig 7 (linked to Fig 3): The M-current is present in long axon neurons but not axonless neurons. a and b. Example de-activating M-current recordings obtained under voltage-clamp conditions using perforated patch-clamp from the somata of granule cells with long axons and axonless neurons respectively in the presence of tetrodotoxin (1 μM), 4-aminopyridine (100 μM) and nickel chloride (1 mM). Cells were held at a fixed potential of -20 mV and 2s hyperpolarizing steps from -30 mV to -110 mV in 10 mV increments were then applied as shown in the schematic. Currents were recorded before (control) and after 15 min bath application of 3 μM XE991. The outward holding currents are indicated on the traces. The scale shown for the raw traces in **a** applies to all unsubtracted traces in **a** and **b**. The currents obtained in the presence of XE991 were then subtracted from those recorded in the absence to isolate the M-current (far right traces; see **Experimental Procedures**). The scale bars shown for the M-current in **a** apply to that in **b**. Once recordings had been obtained, the patch was ruptured and whole-cell mode achieved to fill the neuron with neurobiotin. Post-hoc morphological analysis was done to verify the axon length. **c** Graph depicting the average M-current amplitude (I_M amp) recorded with a hyperpolarizing step from -20 mV to -50 mV in long axon (LA) and axonless neurons. The numbers of observations for each neuron subtype are shown in parenthesis. **d** The apparent activation curve of the M-current in long axon neurons produced from experimentally derived conductance values. This was constructed using the methods described in Shah et al. (2008, PNAS, 105, 7869). **e**. The average fast de-activation time constants of the M-current recorded at varying voltages (V_M).
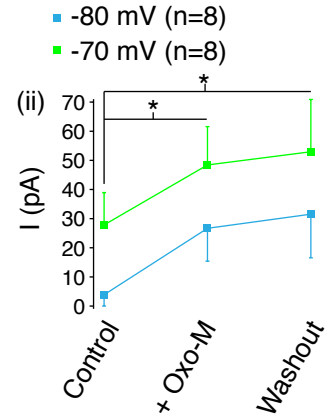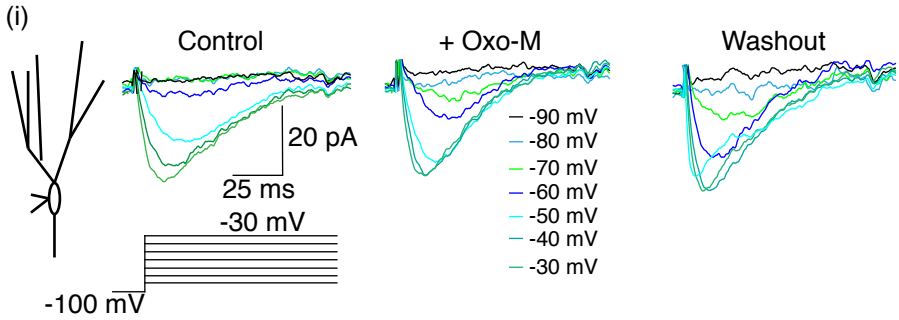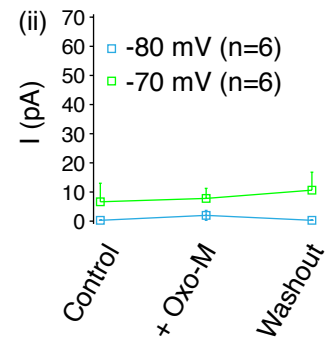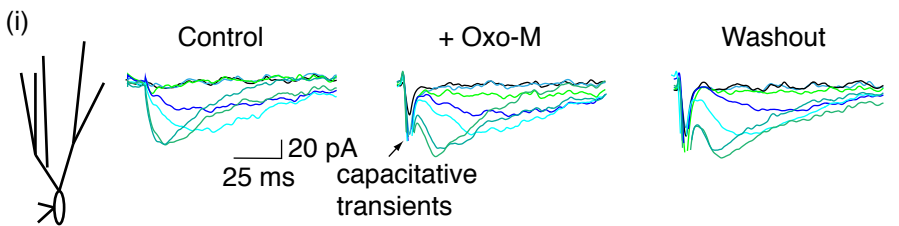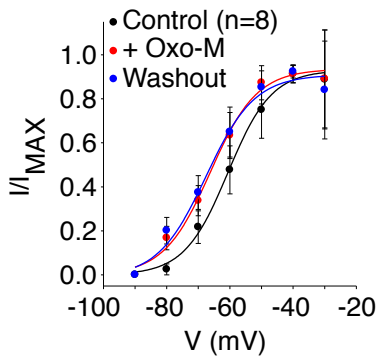
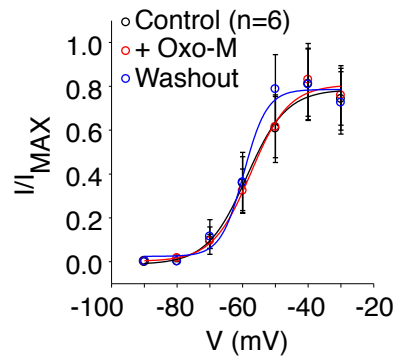**Supp Fig 8: Muscarinic-receptor activation causes sustained enhancement of T-type Ca^{2+} channels**. **a(i), b(i)** Example T-type Ca^{2+} currents recorded under control conditions, after 10 min 1 μM Oxo-M application and following 25 min washout of Oxo-M in long axon and axonless neurons respectively. Cells were held at -100 mV and 1 s, depolarizing pulses from -90 mV to -30 mV as shown in the schematic were applied in the absence and presence of TTA-P2 (500 nM). The difference currents (T-type Ca^{2+} currents) are displayed in **a(i)** and **b(i)**. The currents obtained by stepping to -80 mV and -70 mV are shown in blue and green respectively. **a(ii)**, **b(ii)** The amplitude of currents obtained by stepping to -80 mV and -70 mV from -100 mV before, during and 25 min after Oxo-M treatment. **c, d** The activation curves obtained under control conditions, with Oxo-M and after 25 min washout of Oxo-M in long axon and axonless neurons respectively. Asterisks represent significance at $p < 0.05$ compared with controls.

Supp. Table 1 (Linked to Figs 1, 2, 4, 5, 6; see spreadsheet): Comparison of action potential amplitudes and widths following cholinergic stimulation and muscarinic receptor activation. Summary of changes in action potential (AP) amplitude (amp) and width caused by either optical or electrical stimulation of cholinergic axons or by application of Oxo-M in long axon (LA) neurons and axonless neurons. The effects of cholinergic afferent electrical stimulation in the presence of the anticholinesterase inhibitor, neostigmine and the nicotinic receptor blockers, methyllycaconitine (10 nM) and hexamethonium (200 μM) or when atropine (3 μM) was added to the washout are reported. In addition, the effects of either cholinergic fiber electrical stimulation or co-application of Oxo-M and the K_V7 channel inhibitor, XE991, the Ca^{2+} chelator, BAPTA, the water soluble PIP_2 analogue, diC8-PIP_2, or the Ca^{2+} channel inhibitors, cadmium chloride ($CdCl_2$), TTA-P2, nickel chloride ($NiCl_2$) and SNX482 on spike characteritics are shown. The numbers of observations are indicated in parenthesis.

Supp. Table 2 (linked to Figs 1, 2, 4, 5, 6; see spreadsheet): Effects of cholinergic fiber stimulation and Oxo-M on RMP, R_N and ADP in the absence and presence of pharmacological inhibitors. Summary of changes in resting membrane potential (RMP) and input resistance (R_N) when cholinergic fibers were either electrically or optically stimulated at high (27.8 Hz) or low (0.8 Hz) frequency in the absence or presence of the anticholinesterase inhibitor, neostigmine, nicotinic receptor blockers (methyllycaconitine (10 nM) and hexamethonium (200 µM)), the addition of atropine (3 µM) after stimulation, the $K_V 7$ channel inhibitor, XE991 and the T-type Ca^{2+} channel inhibitor, TTA-P2. Also shown are the alterations in RMP and R_N with Oxo-M in long axon (LA) neurons and axonless neurons when bath applied or focally applied either alone or together with XE991, the PIP_2 modulator, diC8-PIP_2, the Ca^{2+} chelator, BAPTA or the Ca^{2+} channel inhibitors, cadmium chloride ($CdCl_2$), TTA-P2, nickel chloride ($NiCl_2$) and SNX482. The effects of these treatments on the area and amplitude of the afterdepolarization induced by Oxo-M application are also reported. Asterisks indicate significant ($p < 0.05$) differences when compared with Oxo-M alone. All effects were reversible upon washout of the compounds. The numbers of observation for each value are indicated in parenthesis.

Martinello et al., 2014, Supp. Table 3 (linked to Fig 2)

	RMP (mV)	R_N (MΩ)
Long Axon Neurons	-80.36 ± 0.2 mV (n=136)	297.94 ± 23.9 (n=117)
Axonless Neurons	-80.14 ± 0.48 mV (n=15)	201.41 ± 15.89 (n=15)

Supp. Table 3: Comparison of intrinsic membrane properties of neurons with and without axons. Table depicting the average resting membrane potential (RMP) and input resistance (R_N) of neurons with intact axons (long axon neurons) and axons with an average axon length of 6.1 ± 1.2 μm (n=18; axonless neurons). The numbers of observations for each parameter are indicated in brackets.

Martinello et al., 2014, Supp. Table 4 (linked to Fig 3)

	Control RMP (mV)	RMP in the presence of modulator (mV)	Control R_N (MΩ)	R_N in the presence of modulator (MΩ)	Control AP amp (mV)	AP amp in the presence of the modulator (mV)	Control AP width (ms)	AP width in the presence of the modulator (ms)
XE991, 3 µM, LA neurons	-80.70 ± 0.97 mV (n=10)	-79.25 ± 1.05 mV (n=10)	251.92 ± 33.0 MΩ (n=10)	264.62 ± 34.0 MΩ (n=10)	74.80 ± 2.88 mV (n=10)	75.29 ± 3.25 mV (n=10)	1.34 ± 0.11 ms (n=10)	1.48 ± 0.09 ms (n=10)
XE991, 3 µM, axonless neurons	-79.68 ± 0.5 mV (n=8)	-80.22 ± 1.15 mV (n=8)	183.01 ± 20.1 MΩ (n=8)	181.85 ± 19.0 MΩ (n=8)	78.39 ± 2.26 mV (n=8)	78.52 ± 1.91 mV (n=8)	1.83 ± 0.09 ms (n=8)	1.9 ± 0.07 ms (n=8)
ABP (8 mM), LA neurons	-80.63 ± 0.53 mV (n=6)	-80.56 ± 0.41 mV (n=6)	348.88 ± 29.8 MΩ (n=6)	373.05 ± 28.3 MΩ (n=6)	75.92 ± 3.94 mV (n=6)	74.13 ± 1.89 mV (n=6)	1.54 ± 0.07 ms (n=6)	1.60 ± 0.04 ms (n=6)
sABP (8 mM), LA neurons	-79.79 ± 0.96 mV (n=8)	-79.83 ± 1.10 mV (n=8)	311.68 ± 33.1 MΩ (n=8)	318.51 ± 33.2 MΩ (n=8)	71.86 ± 1.10 mV (n=8)	70.22 ± 1.94 mV (n=8)	1.35 ± 0.07 ms (n=8)	1.45 ± 0.06 ms (n=8)

Supp. Table 4: Effects of K_V7 channel inhibitors on granule cell intrinsic membrane properties. Comparison of the resting membrane potential (RMP), input resistance (R_N) and action potential (AP) amplitude (amp) and width in the absence (control) and presence of XE991 in long axon (LA) neurons and axonless neurons. The effects of the ankyrin G binding peptide (ABP) and scrambled ABP were also compared. For ABP and sABP, control recordings were those acquired within 2 min of achieving whole-cell mode. Full effects of ABP and sABP occurred within 25 min of achieving whole-cell configuration (**Fig 3**). The numbers of observations for each group are indicated in parenthesis.

<u>Supplementary Movie S1 (linked to Fig 2)</u>

Cholinergic fibers within the granule cell layer are in close proximity to dentate GC AISs. Movie shows a series of images acquired with a z-interval of 0.3 μm. As shown, the GC layer volume is mainly filled by GC somata (NeuN, purple). AISs (primarily from GCs) are clustered in columnar slots between the somata. While the molecular layer and hilus contains a greater overall density of ChAT labeled cholinergic fibers (see Supplementary Fig 3), the ChAT puncta within the GC layer are abundant near the βIV-spectrin labeled AISs (red). Arrows point to examples where cholinergic fibers closely adjoin bundles of AISs. Dimensions (μm): 133.3 w x 61.5 h x 10.5 d.